Measurements of the Temporal and Spatial Phase Variations of a 33 GHz Pulsed Free Electron Laser Amplifier and Application to RF Acceleration

by

Pavel S. Volfbeyn

Submitted to the Department of Physics
in partial fulfillment of the requirements for the degree of

Master of Science

at the

MASSACHUSETTS INSTITUTE OF TECHNOLOGY

December 1994

Autnor .....
Department of Physics
December 18, 1994

Certifie .....
George Bekefi
Professor
Thesis Supervisor

Accepted by .....
George F. Koster
Chairman, Departmental Committee on Graduate Students

Measurements of the Temporal and Spatial Phase Variations of a 33 GHz Pulsed Free Electron Laser Amplifier and Application to RF Acceleration

by

Pavel S. Volfbeyn

Submitted to the Department of Physics
on December 18, 1994, in partial fulfillment of the
requirements for the degree of
Master of Science

Abstract

In this thesis we report the results of temporal and spatial measurements of phase of a pulsed free electron laser amplifier (FEL) operating in combined wiggler and axial guide magnetic fields. The 33 GHz FEL is driven by a mildly relativistic electron beam (750 kV, 90-300 A, 30 ns) and generates 61 MW of radiation with a high power magnetron as the input source. The phase is measured by an interferometric technique from which frequency shifting is determined. The results are simulated with a computer code.

Experimental studies on a CERN-CLIC 32.98 GHz 26-cell high gradient accelerating section (HGA) were carried out for input powers from 0.1 MW to 35 MW. The FEL served as the r.f. power source for the HGA. The maximum power in the transmitted pulse was measured to be 15 MW for an input pulse of 35 MW. The theoretically calculated shunt impedance of 116 $M\Omega/m$ predicts a field gradient of 65 MeV/m inside the HGA. For power levels > 3 MW the pulse transmitted through the HGA was observed to be shorter than the input pulse and pulse shortening became more serious with increasing power input. At the highest power levels the output pulse length (about 5 nsec) was about one quarter of the input pulse length. Various tests suggest that these undesirable effects occur in the input coupler to the HGA. Light and X-ray production inside the HGA have been observed.

Thesis Supervisor: George Bekefi
Title: Professor

Acknowledgments

I want to thank George Bekefi for all the things he taught me and for his patience in advising me throughout the three and a half years I have worked with him.

I thank Ivan Mastovsky for without him not a thing would work in the lab, for all the help and advise he gave me.

I am grateful to my wonderful officemate and friend Gennady Shvets for all the physics and other things I learned in our discussions with him and for being such a great friend.

I wish to thank Jonathan Wurtele for all the advise he gave me and for helping me with this thesis.

I thank Beth Chen for doing so much of the work for me and for her friendship.

I am greateful to Manoel Conde for building the FEL and helping me to start working at the lab.

I thank Ken Ricci for working with me on the Phase Shift measurements.

I am thankfull to Felicia Brady, Palma Catravas and Wen Hu for being the great coworkers they are.

And last but not least I thank my parents who started me and carried me through most of my Physics education.

Contents

List of Figures

List of Tables

Chapter 1

Introduction

1.1 Introduction

Free electron lasers are by now well studied sources of electromagnetic radiation that use the kinetic energy of free electrons to produce light. The coupling of the electron energy into radiation is achieved by making the electron beam oscillate in the plane perpendicular to the direction of the electron beam propagation by the action of a periodic transverse magnetic field provided by a wiggler device. The combined action of wiggler and r.f. fields on the beam causes axial bunching of electrons that makes them radiate coherently. Section 2 of Chapter 1 of this thesis presents a simple physical picture of the FEL interaction. In Section 3 of Chapter 1 the application of the FEL to High Gradient acceleration is discussed. Section 4 of Chapter 1 and section 1 of Chapter 2 describe the MIT 33 GHz FEL, its design features and parameters. Some comprehensive review papers [1, 2, 3] will give a reader a good feeling for FEL physics and describe important developments in the field up to date. They also include an extensive bibliography.

Two advantages of FELs with respect to the conventional atomic and molecular lasers are tunability of the radiation frequency and the absence of a fragile lasing medium. The absence of atoms or molecules is responsible for the high power handling capability of the device. Frequency tuning, achieved by changing the energy of the electron beam or the wiggler field, is crucial for a number of applications of the FELs,

high gradient r.f. acceleration among them.

Sensitivity to phase jitter of r.f. driven accelerators imposes a strict requirement on FEL phase stability. FEL sources have been proposed [4] with an extremely tight requirement on the bandwidth of the radiation and, for acceleration applications, on its phase and its shot to shot repeatability. One of the goals of this experiment was to try to deal with this question. Also the recent reports of frequency upshifts in FEL [5, 6, 7] prompted this more detailed temporal measurement of phase. The experiment and results from a study of phase shift in the MIT 33.39 GHz FEL are described in Chapter 2 along with a qualitative theoretical explanation and some results from numerical simulations [8].

There is great interest in today's high energy physics community to push the limit of particle acceleration to ultra high electron energies (> 1 TeV). However, by the standards of present day accelerators which generate accelerating gradients of at most 17 MV/m (SLAC), a device with length of the order of hundreds kilometers would be necessary. One of the alternatives is to increase the accelerating gradient.

In the types of accelerators used currently, the maximum radiation power one can use for acceleration is limited by energy requirements and r.f. breakdown. One of the ways to reduce energy needs and increase the r.f. breakdown threshold is to increase the frequency of the r.f. drivers. This requires novel high power sources as for example the free electron lasers. Thus, as a part of CERN-CLIC project, a 32.98 GHz (to be compared with 3 GHz used at SLAC) accelerating structure was manufactured. It was designed to achieve 80 MV/m gradient for input powers of 30 MW easily available with the MIT FEL. Chapter 3 presents the experimental results of high gradient testing of the CERN-CLIC 32.98 GHz accelerating section.

1.2 FEL theory

A brief theoretical presentation of Free Electron Laser (FEL) will be given in this section. For an excellent, detailed review of FEL theory and recent experiments, please refer to reference [2].

An FEL is a device that transfers a part of the kinetic energy of a relativistic beam of free electrons into the energy of a radiation field. To achieve coupling between the electron beam and the electromagnetic radiation the electrons are made to oscillate transversely (in the plane perpendicular to the direction of beam propagation) by action of transverse periodic static or r.f. magnetic fields produced by a *wiggler* device.

To better understand the nature of the interaction let us imagine that a monoenergetic electron beam is propagating in a wiggler field with spatial period of oscillation λ_w (i.e. a transverse magnetic field that changes as $\vec{B}_w = \hat{j}B_w cos(\frac{2\pi}{\lambda_w}z)$, where z is in the beams direction of propagation). Let each electron in the beam be characterized by a relativistic energy factor of $\gamma = \sqrt{\frac{1}{1-v^2/c^2}}$, where v is the axial electron velocity. In the frame where the electrons are stationary the wiggler field acts very much like a plane wave of period λ_w/γ (Lorentz transformation for highly relativistic speeds). This wave is partially scattered back by the electrons. The frequency of this back-scattered wave is further increased by the transformation into the laboratory frame of reference (Doppler effect). Thus the frequency becomes $\frac{2c}{\lambda_w}\gamma^2$. This demonstrates an important issue namely the tunability of the device. By changing γ or λ_w (the latter is rarely an option) one changes the frequency of the radiation produced by the FEL.

To understand the dynamics of the interaction consider the forces that act on the electrons. The wiggler magnetic field makes all electrons describe wiggly (hence the name wiggler) trajectories that oscillate in the transverse plane with the same spatial periodicity as that of the wiggler. Take for example a planar wiggler with the B-field in y direction: $\vec{B}_w = \hat{j}B_w cos(\frac{2\pi}{\lambda_w}z)$. Let the beam of electrons propagate in the z-direction. The electrons will experience a force in the x direction proportional to $B_w cos(\frac{2\pi}{\lambda_w}z)$. As a result the electrons will oscillate in the X-Z plane with a steady-state velocity $v_x sin(\frac{2\pi}{\lambda_w}z)$.

If a radiation wave is present, propagating in z-direction, with its E-field in x-direction $\vec{E} = \hat{i}Esin(\omega t - kz + \phi)$, and the B-field $\vec{B} = \hat{j}Bsin(\omega t - kz + \phi)$, the electrons will experience a $\vec{v} \times \vec{B}$ force in the z-direction that is proportional to

$$F_{\vec{v}\times\vec{B}} \sim sin(\frac{2\pi}{\lambda_w}z)sin(\omega t - kz + \phi) = \frac{1}{2}(cos(\omega t - (k+k_w)z + \phi) - cos(\omega t - (k-k_w)z + \phi)). \tag{1.1}$$

Where $k_w = \frac{2\pi}{\lambda_w}$. The second term in this equation (as well as several other forces that are not considered here) oscillates with a very high frequency $\geq \omega$ in the frame of the electrons and thus it barely affects the electrons, but the first term could affect the motion of electrons appreciably if the phase velocity of the force (often referred to as the *ponderomotive* force) is close to the beam velocity. If that is true an electron in the beam will see a nearly constant force as it moves along and the electrons will start to *bunch* in the potential wells of the ponderomotive force. The bunches oscillating in the x-z plane create a net transverse current that will drive the radiation field by coupling to the E-field of the wave. This indicates that the optimum growth of the wave is achieved when

$$\omega = (k + k_w)v_z. \tag{1.2}$$

Equation (1.2) is far from complete in describing an FEL. To obtain a more accurate description of FEL interaction other important phenomena such as the space charge force, finite physical dimensions of the electron beam, and the guide magnetic field must be taken into consideration.

From linear theory it is possible to derive a FEL dispersion relation. It relates the wavenumber k of an electromagnetic wave and its frequency ω when interacting with a beam of free electrons with initial energy $\gamma_0 = (1 - {v_{z0}}^2/c^2)^{-\frac{1}{2}}$ and particle number density n_0 in a presence of a wiggler of period $2\pi/k_w$ that creates a field B_w. For a helically polarized wiggler field in a one-dimensional representation [2] the dispersion relation is

$$\left[k - \left(\frac{\omega^2}{c^2} - F\frac{\omega_b^2}{\gamma_0 c^2}\right)^{1/2}\right]\left[\left(k + k_w - \frac{\omega}{v_{z0}}\right)^2 - \frac{P_1\omega_b^2}{{v_{z0}}^2\gamma_0\gamma_z^2}\right] = -F\frac{\omega_b^2/c^2}{2\gamma_0}\beta_w^2(v_{z0}/c)^{-2}k_w. \tag{1.3}$$

Where c is the speed of light, F is the "filling factor" associated with the radiation field, $\omega_b = 4\pi|e|^2 n_0/m_0$ is the electron beam plasma frequency, $\gamma_z = (1 - \frac{{v_{z0}}^2}{c^2})^{-\frac{1}{2}}$,

$\beta_w = |e|B_w/(k_w\gamma_0 m_0 c^2)$ is the normalized electron wiggle velocity, P_1 is a space-charge reduction factor.

This dispersion relation has three roots for a given set of parameters. They correspond to three possible k numbers for a fixed value of ω (assumed to be real). Each such k number describes an electromagnetic wave with fields that change as $E = E_0 e^{i(kz-\omega t)}$. The roots could be all real, corresponding to propagation without growth or decay. For a certain set of FEL parameters two of the roots could come out complex. One of the two would correspond to an exponentially growing wave, while the other would describe an exponentially decaying solution.

Two distinct limits corresponding to different relative values of current density and of the wiggler field strength exist. When the current is low and the wiggler field is high the dispersion relation takes a form of a cubic. This is called the high gain **Compton Regime**. When the electron beam current density is high the dispersion relation takes a form of a quadratic. This is known as the **Raman Regime**. A more detailed discussion and a comparison of these two regimes is given in Section 1 of Chapter 2.

Let us assume that the FEL is tuned so that the dispersion relation has a root that corresponds to a growing wave. It could be written in a form of $k = \omega/c - \Delta k$. The imaginary part of Δk determines how fast the wave amplitude will grow spatially (ω is taken to be purely real). (The rate of the growth of the wave's intensity (the *growth rate*) is $\Gamma = 2Im\Delta k$.)

The real part of Δk corresponds to shift in the wavenumber, and, after many exponentiation lengths, gives a phase shift $\Delta\phi = Re\Delta kl$ (after propagating for a distance l). This phase shift of the radiation pulse is similar to that in a dielectric medium (such as glass or air). If the refraction index of such medium is n then we define the phase shift acquired over a distance l to be $\Delta\phi = -\frac{2\pi(n-1)l}{\lambda}$, where λ is the wavelength of the radiation in vacuum. The phase shift defined in this way (with a minus sign) is convenient for the discussion of frequency shifts in the Chapter 2 (see for example equation (2.22)).

The FEL interaction changes the index of refraction in a more complicated manner

than a dielectric. The phase shift depends on the beam energy, wiggler period and strength, guiding field strength, and other parameters as well as the electron beam plasma frequency (density). This is the phase shift that was measured as a part of the experiment described in this thesis.

1.3 Application of the FEL to Acceleration

To date the most common device used for electron acceleration is the linear r.f. accelerator. A typical linear accelerator is a slow wave or a standing wave structure powered by an r.f. source. The radiation input into the structure creates electric field gradients inside the structure that accelerate electrons. The r.f. fields oscillate with high frequencies ($\sim 1 - 3$ GHz). An electron in such field cannot be effectively accelerated because the field direction and hence the accelerating force direction are apt to change quickly unless some special measures are taken. In case of a standing wave accelerator one introduces a shift in phase of electric field oscillation between the adjacent cavities, such that the electron as it leaves one cavity is continued to be accelerated in the same direction by the field in the next one. Traveling wave accelerators utilize slow wave structures to decrease the phase velocity of the r.f. wave to the speed of light or less. Then energetic electrons (with velocities close to the speed of light) can stay on the crest of the accelerating wave for many r.f. oscillations.

A useful quantity for describing accelerating structures is the shunt impedance. It determines the accelerating field gradient inside a structure for a given r.f. input power. It is a function of the geometry of the structure, the mode, and the frequency of the r.f. For a shunt impedance r and input power P one determines the maximum accelerating electric field on axis of the structure, of magnitude E, by

$$E \sim \sqrt{rP}. \tag{1.4}$$

(The fields at the surface of the structure are considerably larger).

The higher the driver frequency the smaller the size of the structure (it scales

linearly with the r.f. wavelength for a given design). The smaller the size of an accelerator the higher the shunt impedance. The reason is that if the same amount of energy is injected into a smaller volume, the field inside that volume will be greater. The fields inside a structure are proportional to the square root of the power devided by the crossectional area of the structure. The crossectional area of the structure is porportional to the r.f. wavelength squared. Thus from the accelerating field scales with the frequency ω and the power P as

$$E \sim \omega P^{1/2}. \tag{1.5}$$

The performance of r.f. accelerators is limited by the r.f. breakdown of the accelerating structures. The maximum achievable accelerating gradient scales favorably with frequency. Although data for short pulses at high frequency is sparse, the scaling is expected to roughly follow the semi-empirical relation of Kilpatrick [9]

$$W[E^2 exp(-K_1/E)] = K_2, \tag{1.6}$$

where W is the maximum possible ionic energy (dc or r.f.) in electron volts, E is the electric cathode gradient, $K_1 = 1.7 \times 10^5$ V/cm, and $K_2 = 1.8 \times 10^{14}$. The relationship (1.6) is valid for r.f., d.c. and pulsed d.c. fields. In the r.f. case, the maximum possible ionic energy must include transit-time and phasing effects [9]. For a given gradient the maximum possible energy W that a charged particle can aquire decreases rapidly with the frequency: the higher the frequency of the r.f. the less time there is for the charge carriers inside the structure to be accelerated to sufficiently high energies to cause an avalanche-like current growth (r.f. breakdown) by secondary emission or other processes.

The above discussion illustrates that the accelerating gradient can be maximized by designing a structure that can be driven by a source with the combination of high input power and high r.f. frequency. The demand for ultra-high electron energies (gradients) pushes the development efforts into the high frequencies, up to $\sim$ 100 MV/m and higher.

However, the power of conventional r.f. sources (klystrons, TWT's) decreases dramatically with increasing frequency. It was only in recent years that FELs were discovered to radiate up to 1 GW at microwave frequencies, making them a very attractive power source for High Gradient Accelerators (HGAs) [10]. Table 1.1 is a summary of r.f. devices-candidates for driving HGAs. After the demise of the ELF experiment at LLNL, MIT's FEL stands alone as a high power r.f. source in the frequency range higher than 20 GHz. And thus when a slow-wave structure was being developed at 33 GHz by the CERN/CLIC group it was decided to begin a collaboration with MIT.

This structure is a prototype of a single section of a novel two-beam accelerator that is being developed by the CERN/CLIC group [11, 12]. In this accelerator the energy from a beam with a large current density of 3-5 GeV electrons, drive beam, will be coupled to a high energy electron beam with a much smaller current density. The transfer will be achieved by converting the energy of the drive beam into r.f. radiation of $\sim$ 30 GHz frequency and then accelerating the electrons in the high energy beam in slow-wave accelerating high-gradient r.f. structures similar to the one described in this thesis.

1.4 The Experiment

1.4.1 Summary

If the FEL is to meet the stringent phase and frequency stability requirement of an r.f. driver its phase behavior must be fully characterized and controlled. We have performed detailed spatial and temporal phase measurements of our FEL.

In Chapter 2 of this thesis we describe phase measurements on the FEL. A brief theoretical description of the important FEL physics for our study is presented in section 2.1. A description of different regimes of FEL operation is given, and their main physical features and differences are highlighted. In section 2.2 the experiment and the experimental results are described and a comparison with numerical simulations

Type of amplifier/ (Research Institution)	f (GHz)	V (kV)	P (MW)	τ (μs)	η (%)	l (m)
SLC Klystron (SLAC)	2.856	350	65	3.5	45	0.59
X-Band klystron (SLAC)	11.4	447	50	1.0	22	1.8
Gyroklystron (UMD)	9.85	425	27	1.4	32	1.0
FEL (MIT)	32.99	750	61	0.02	27	0.53
EIK (SRL/Haimson/MIT)	11.4	440	100	0.05	43	0.24
TWT (Cornell U.)	8.76	800	200	0.1	24	0.62

Table 1.1: A summary of amplifier candidates for HGA testing.*

*Adapted from: V.L. Granatstein and C.D. Stiffler "Advanced Accelerator Concepts,"J.S. Wurtele, Editor (AIP Press, 1992) p. 16.

is presented.

Chapter 3 is devoted to the description of the CERN/CLIC HGA testing with the FEL as a driver. The goal of this test is to find the highest power level the structure could support without breakdown (or some other process that would make it unsuitable for electron acceleration) and to study the process. Section 3.1 describes the experimental setup for the testing. Section 3.2 presents the results of high power testing as well as the X-ray and light emission studies. An undesirable pulse shortening was found to take place at high power levels. In section 3.3 we present the results of various tests designed to isolate where the shortening occurs. Section 3.4 describes the results of a test of the feasibility of "conditioning", that is, improving the performance of the HGA by taking repetitive power shots with the FEL. There appears to be evidence that conditioning may improve the HGA's performance. Conclusions are in Chapter 4.

The rest of this Chapter contains a description of the FEL and the HGA and their characteristics.

1.4.2 MIT FEL

A schematic of the Free Electron Laser amplifier setup is shown in figure 1-1.

The mildly relativistic electron beam (750 ± 50 keV, 30 ns) of the FEL is produced by a Physics International pulse generator (Pulserad 110A). It consists of a Marx capacitor bank followed by a Blumlein transmission line. In the Marx, twenty-two 0.1 mF capacitors are charged in parallel and discharged in series by triggered SF6 pressurized spark gaps. Although the capacitors are connected in series by the spark gaps, the SF6 keeps the gaps open (i.e.: in parallel) until triggered. The voltage thus generated proceeds down the Blumlein pulse-forming line to a hemispherical graphite cathode where electrons are emitted by an explosive field emission process. The electrons travel through a concave-faced anode of length 62 mm and radius 2.54 mm. The anode, located 8 mm from the cathode serves as the emittance selector, limiting the Larmor radius of accepted electrons. Less than 2% of the electrons generated passes through the anode and into the interaction region (a circular drift tube of

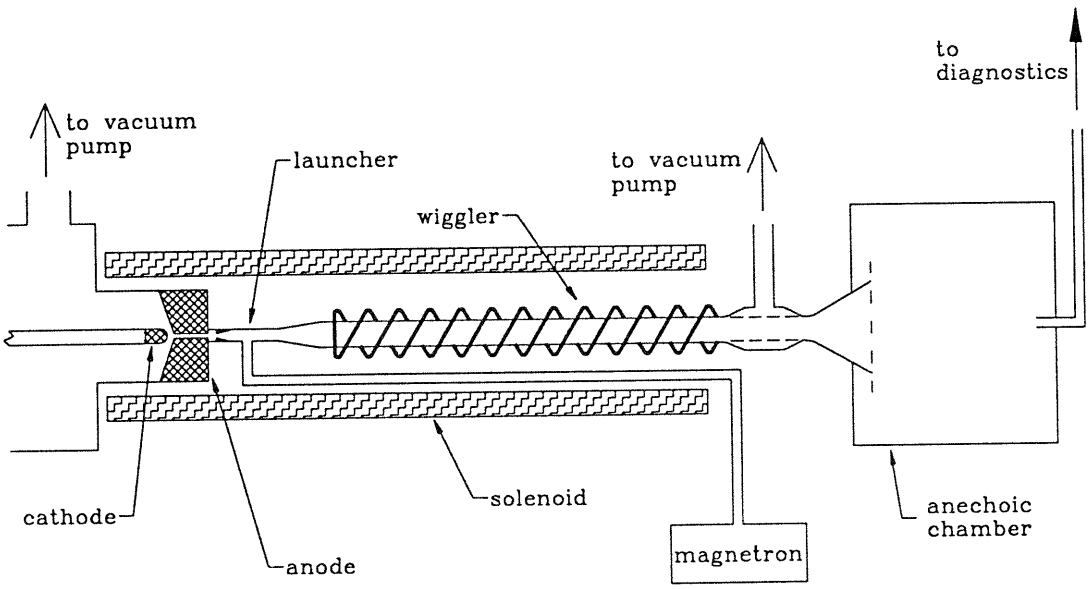

Figure 1-1: The schematics of the FEL set-up.

inner radius 0.51 cm).

The 2 meter long stainless steel drift tube is located inside a 50 period, bifilar (double helix, concentrically wound) wiggler magnet. Current in each helix flows in the opposite direction resulting in zero net axial field. The remaining net transverse field of the wiggler rotates with the periodicity of the helix (3.18 cm). To insure that the electrons enter the drift tube adiabatically, the wiggler is up-tapered in amplitude over the first six periods. The on-axis wiggler field can be adjusted up to 1.8 kG. A high power magnetron provides the input r.f. radiation to be amplified by the FEL. It operates at 33.39 GHz for the phase shift measurements and 32.9659 GHz for the HGA measurements. The technique for calibrating the frequency of the magnetron is described in section 3.2. The linearly polarized microwave radiation from the magnetron has approximately 40 kW of power. It is injected in the interaction region via a wave launcher. The wave launcher is a short section of a circular waveguide of 0.31 mm in radius which supports only the fundamental $TE_{1,1}$ mode at the operating frequency. It is adiabatically up-tapered to the drift tube radius, thereby injects a linearly polarized wave into the FEL. The drift tube, with a cut-off frequency of 17.2

Parameter	Group I	Group II	Reversed Field
Driver frequency (GHz)	33.39	33.39	33.39
Beam energy (keV)	750	750	750
Beam current (A)	90	300	300
Guide field (kG)	4.06	10.9	-10.9
Wiggler field (kG)	0.63	0.63	1.47
Maximum power (MW)	5.8	4.2	61
Normalized RMS emittance (cm-rad)	$2.3\text{x}10^{-2}$	$2.3\text{x}10^{-2}$	$2.3\text{x}10^{-2}$
$\Delta\gamma_z/\gamma_z$ (percent)	0.4	0.4	0.4
v_z/c (calculated)	0.898	0.898	0.911

Table 1.2: A summary of the MIT's FEL parameters. $\Delta\gamma_z/\gamma_z$, the rms spread in the longitudinal energy of the beam electrons, and the rms emittance are defined in reference [7], v_z/c is the normalized electron axial velocity component calculated for the stable orbits of electrons with energy of 750 keV.

GHz, acts as a circular waveguide for the radiation for the rest of the interaction region. The cathode, anode, drift tube, and wiggler are all immersed in focusing axial magnetic field generated by a solenoid. This field can be adjusted up to 11.6 kG.

The system (electron gun and drift tube) is maintained under a vacuum of $< 10^{-5}$ Torr during operation. This is made possible by two turbo-molecular pumps, one located near the FEL diode and the other at end of the drift tube.

The summary of the FEL's operating parameters is given in Table 1.2. Three different regimes of FEL operation are described in subsection 2.1.1.

1.4.3 HGA

The 32.98 GHz disc-loaded constant gradient traveling-wave accelerating structure was built as a prototype of an element in the accelerating line of the two-beam CERN-CLIC accelerator. It is a $2\pi/3$ mode, $v_p = c$ constant gradient iris disc-loaded waveguide structure. It consists of 26 cells, each of 3.029 mm in length and 2 coupler cells 3.56 mm long. The total length of the structure is 0.08587 m. The fill time of the structure is 3.42 ns, with the group velocity of 0.083c. The two side-couplers are at right angles to the axis of the structure. They couple the power from a standard Ka-band rectangular waveguide into the desired mode of the structure. The HGA possesses a wide transmission band of about 500 MHz. However for acceleration purposes the frequency must be held at 32.988 GHz with possible variations of less than 1 MHz. A photograph of the HGA is shown in figure 1-2.

The high vacuum of around 1×10^{-7} Torr is maintained by two 30 liters/sec ion-pumps. The structure was designed to have shunt impedance of 116 MΩ/ m. This means that for the input power level of 30 MW the maximum accelerating gradient is approximately 80 MV/m.. Some of the key parameters of the HGA are shown in Table 1.3.

A schematics of the experimental setup for powering the HGA with the MIT's FEL is presented in figure 1-3. The radiation output of the FEL is mode-converted to match the input coupler of the HGA and the transmitted radiation is dumped in a reflection-free chamber. A more detailed description of the setup is found in section 2 of Chapter 3.

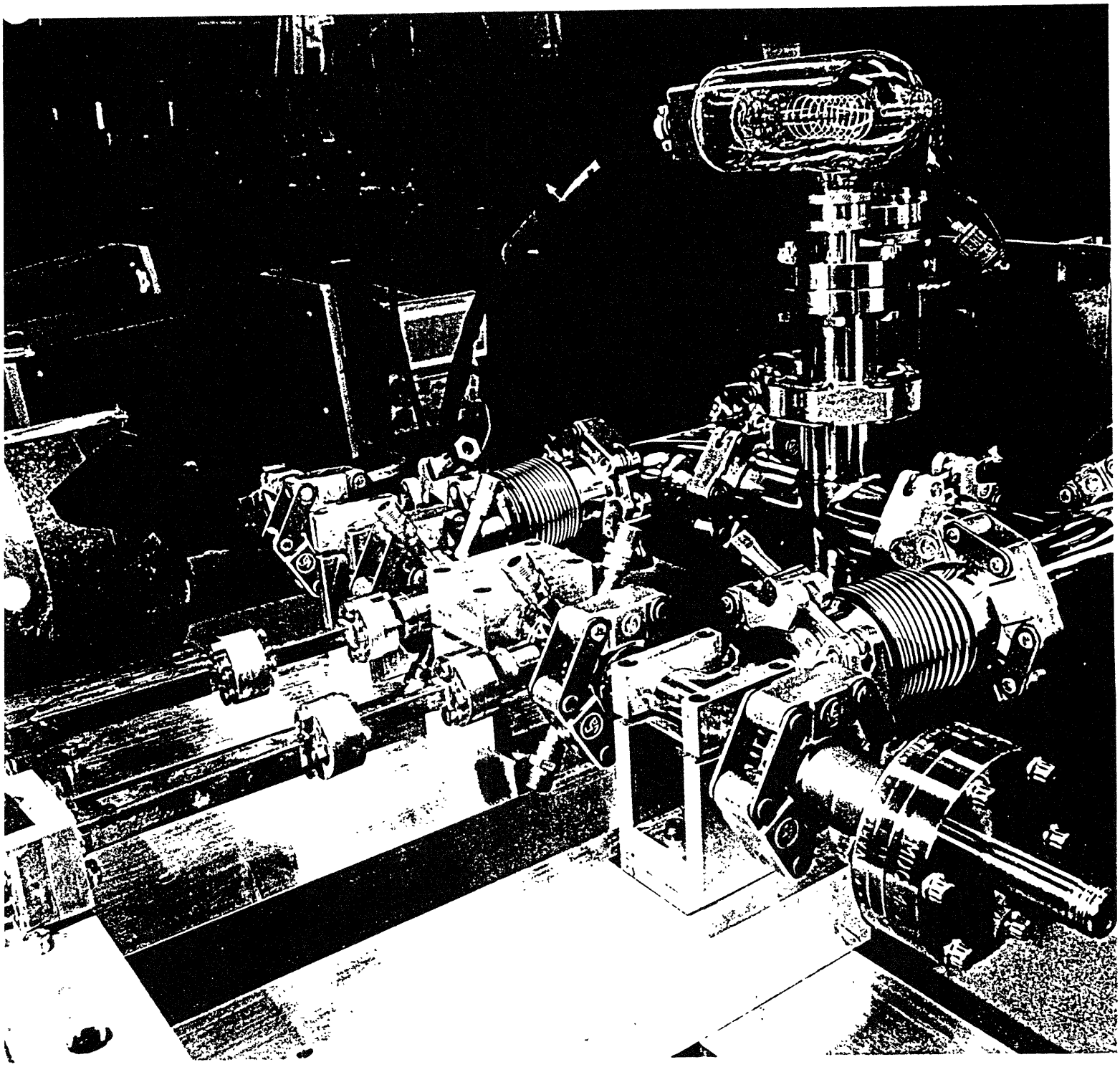

Figure 1-2: HGA. Installed with the pumping manifold and incoming and outcoming waveguides.

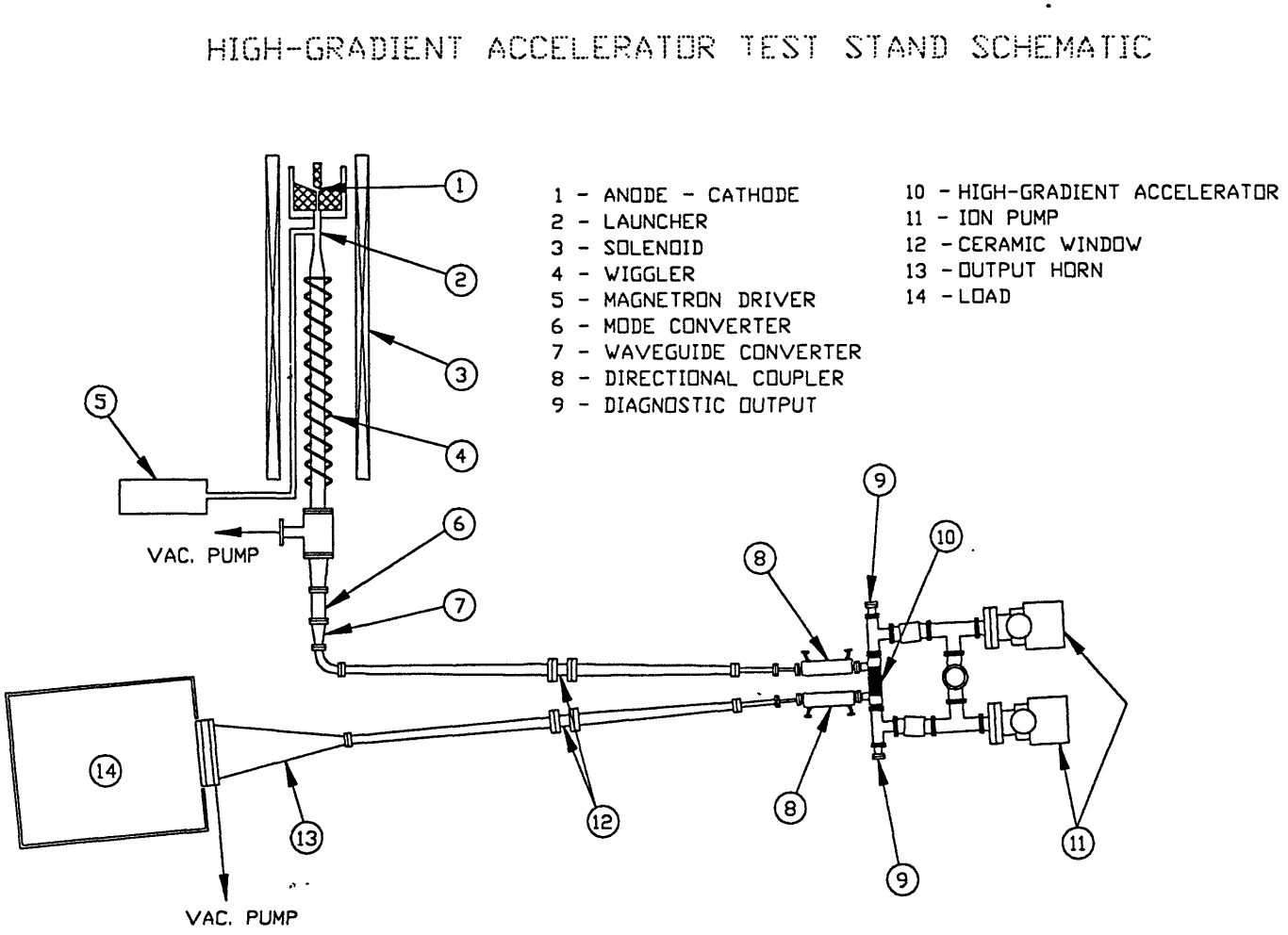

Figure 1-3: The schematic of the HGA testing setup.

frequency	f	32.988 GHz
wavelength	λ	0.009088m
cell length	$L_c=\lambda/3$	3.029 mm
shunt impedance	r	116 MΩ/m
number of cells	N	26+2
section length	L	0.08587 m
section fill time	t_f	3.33 ns

Table 1.3: A summary of the HGA parameters.

Chapter 2

MIT FEL

2.1 FEL with Axial Guiding Magnetic Field

In practice electrons in an electron beam will always have transverse components to their velocities of random and therefore destructive nature. Among the processes that lead to generation of the transverse velocity components, thermal spread, space-charge induced spread, and spread due to the cathode nonuniformities are the most common. An error of alignment can cause a beam to exit the interaction region prematurely. We use a uniform axial magnetic field to overcome the electrostatic repulsion of the electrons and transport the beam through the wiggler.

This *guide* field $\vec{B}_g = \hat{k}B_z$ not only counterbalances the electrostatic repulsion of the electrons, but also affects, in a very important way, the dynamics of the particles traversing the wiggler magnet and the FEL interaction.

We use a bifilar helical wiggler magnet. It consists basically of two helices of period λ_w that are displaced axially by $\lambda_w/2$ and have electric currents flowing in opposite directions. The resulting wiggler magnetic field $\vec{B}_w$ is essentially perpendicular to the axis of the helices (assumed to be along the z-direction) and rotates with periodicity λ_w. In first approximation this field is

$$\vec{B}_w = B_w[\hat{i}cos(k_w z) + \hat{j}sin(k_w z)] \tag{2.1}$$

when transverse field variations are neglected. Here B_w is the wiggler field amplitude, and $k_w = 2\pi/\lambda_w$.

Electrons propagating in the z-direction and subject to an axial field superimposed on the helical field of equation (2.1) are known to have steady-state orbits [13, 14, 15] with constant, time independent axial and transverse velocities. It is not difficult to find these velocities in a simple, one-dimensional approximation (in which it is assumed that the wiggler field does not have any x or y dependence). As it will be seen later, this is not a bad approximation, but it does not encompass all the important relevant physical phenomena.

These steady orbits must have the same period as the driving wiggler field and so a steady orbit is a helix with period λ_w. The net force acting on an electron on such an orbit is radial and its magnitude is determined by the electrons acceleration as it traverses the helix:

$$\frac{\gamma_0 m_0 v_\perp^2}{r} = e(-v_\perp B_z + v_z B_w), \tag{2.2}$$

where $\gamma_0 = (1 - \frac{v_0^2}{c^2})^{-\frac{1}{2}}$ is the relativistic energy factor associated with the initial electron velocity $\vec{v_0} = \vec{k} v_0$, m_0 is the electron rest mass, $v_\perp$ and v_z are the particle transverse and axial velocities, e is the absolute value of the electron charge, and r is the radius of the orbit (i.e. the radius of the helical orbit in the transverse plane). We have assumed the positive sign for transverse components of the vectors to be in the direction of the wiggler field, and the positive z-axis to be in the direction of the wiggler field helicity (cork-screw like) as shown in figure 2-1.

These helical orbits of period λ_w have angular velocities of $\partial\theta/\partial t = k_w v_z$, from which it follows that

$$k_w r = \frac{v_\perp}{v_z} \tag{2.3}$$

Eliminating r between equations (2.2) and (2.3) leads to the sought-after orbit equation:

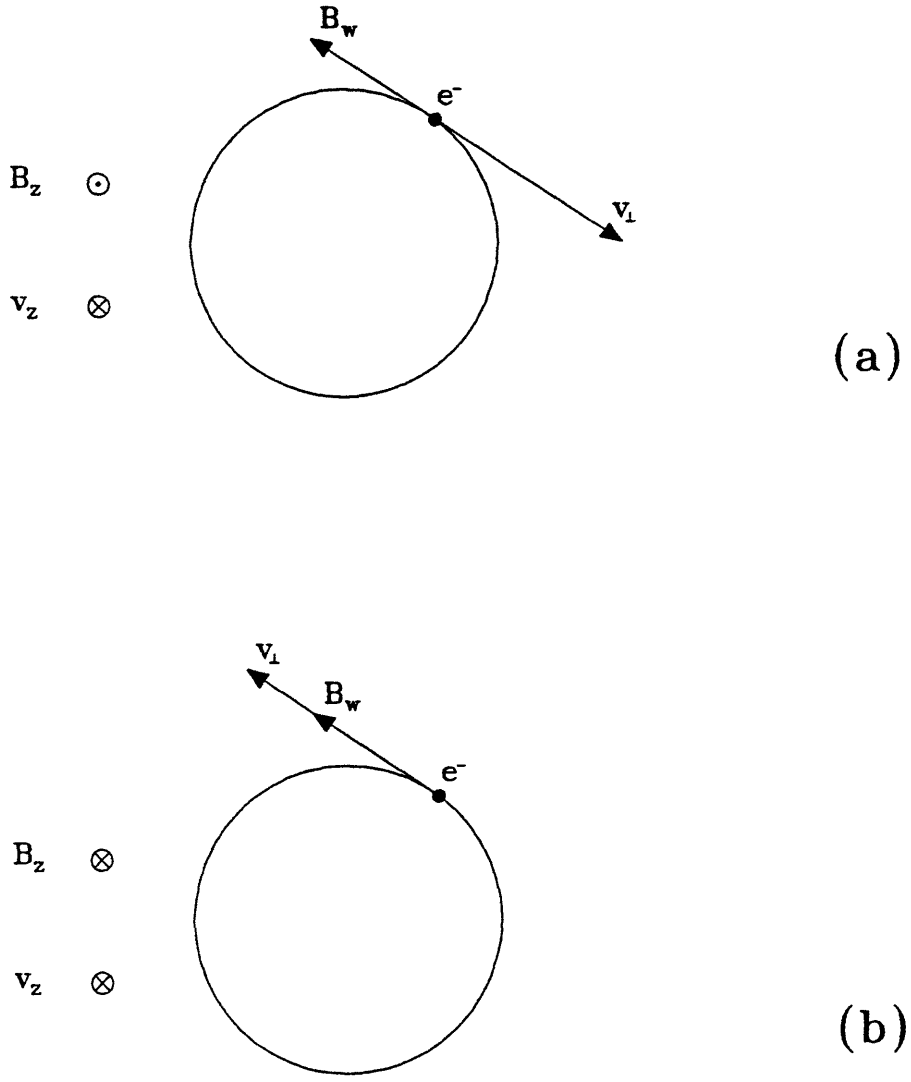

Figure 2-1: Projection of the helical orbits onto the transverse plane (x, y) indicating the directions of $\vec{B_w}$, $\vec{B_z}$, and $\vec{V_z}$. a) With the guide field in the same direction as the wiggler field's helicity. b) Reversed.

$$\alpha \equiv \frac{v_\perp}{v_z} = |\frac{\Omega_w}{k_w v_z - \Omega_z}|, \tag{2.4}$$

where $\Omega_z = eB_z/(\gamma_0 m_0)$ is the relativistic electron cyclotron frequency in the axial field B_z, and $\Omega_w = eB_w/(\gamma_0 m_0)$ is defined by analogy with the cyclotron frequency but with the wiggler field amplitude B_w in place of B_z.

This equation has a singularity at $k_w v_z = \Omega_z$ which corresponds to a resonance-like growth of the transverse velocity component and the orbit radius. This creates an unstable region often called *gyroresonance* where the electrons are driven out of the interaction region by the combined action of wiggler and axial fields. This region divides the steady state orbits into two classes (regimes) **Group I**, when the B_z field is small ($k_w v_z > \Omega_z$), and **Group II** when the guiding field is large such that the cyclotron frequency Ω_z is greater than $k_w v_z$.

There is nothing that should prevent operation at negative axial fields i.e. $\Omega_z < 0$ [7]. The regime with negative guide field, in the direction opposite to the direction of wiggler field helicity, we will call the **Reversed Field** regime. This regime of operation was discovered by M.E. Conde and G. Bekefi [16].

The previous study of this FEL [16, 17, 18, 7] has shown that the FEL performance is at its best in the Reversed Field regime, where an efficiency of 27% (60 MW in power) was achieved. Groups I and II proved to be much less efficient. As one can see from the Table 1.2 , the output powers and efficiencies for these two regimes are much worse than those for the Reversed Field regime. The poor performance in Group I is attributed to particle loss due to closeness of the unstable region. The Group II operation was proved in course of this study to be very dependent on the beam alignment. After realigning the beam in the drift tube it was possible to observe power levels around 10-11 MW, to be compared with 4 MW measured to be the maximum in Group II before alignment. The gyroresonance seems to strongly influence the performance of the FEL.

2.1.1 Realistic Wiggler Model and Finite Beam Thickness

So far we have considered the case of an idealized wiggler (see equation 2.1), whose field has no transverse dependence and an infinitely thin electron beam injected on axis. A realistic representation of the magnetic field generated by a bifilar helical wiggler includes higher order harmonics of the period λ_w and also a radial dependence of the field amplitude. In cylindrical coordinates (r, θ, z), with the helix axis coincident with the z axis, the magnetic field $\vec{B}_w$ can be expressed [14, 19] as

$$\vec{B}_w = -\frac{2\mu_0 i k_w a}{\pi}\nabla[\sum_{m=1}^{\infty} sin(\frac{m\pi}{2})cos(m(\theta - k_w z)) \times K'_m(mk_w a)I_m(mk_w r)], \quad (2.5)$$

where μ_0 is the permeability of free space, i is the electric current in the wiggler, a is the radius of the helices, K'_m is the derivative of the modified Bessel function of the second kind (of order m), and I_m is the modified Bessel function of the first kind (of order m).

The expression for the particle transverse velocity in response to a single harmonic component of the wiggler field was calculated ([20, 21]) to be

$$\frac{v_\perp}{v_z} = n\frac{2\Omega_w I_n(k_w r)}{nk_w(v_z) - \Omega_z - 2\Omega_w I_1(k_w r)I_0(k_w r_g)}I_{n-1}(k_w r_g), \quad (2.6)$$

where n is the harmonic number, and r_g is the radial displacement of the particle guiding center. This is the more general form to be compared with the idealized case given by equation (2.4).

In the case of axis-centered motion ($r_g = 0$), all but the fundamental harmonic component ($n = 1$) vanish, because the Bessel function $I_{n-1}(k_w r_g)$ is zero. For the off-axis electrons the harmonic components are of the order of $(k_w r_g)^{|n-1|}$ for small $k_w r_g$ and, in regions far removed from resonances, the fundamental harmonic is dominant because $k_w r_g \ll 1$ under our experimental conditions.

At and near the harmonic resonances where

$$nk_w v_z - \Omega_z - 2\Omega_w I_1(k_w r) I_0(k_w r_g) \simeq nk_w v_z - \Omega_z \simeq 0, \tag{2.7}$$

$v_{\perp n}$ becomes large (see equation(2.6)) and the dynamics of the particles cannot be calculated from the fundamental harmonic only.

From equation (2.7) one finds that for $n = -1$ there is a resonance for $k_w v_z = -\Omega_z$ (Reversed Field regime). Since it is only the off-axis electrons that are affected by this resonance and the magnetic field amplitude of this $n = -1$ component is much smaller that the fundamental harmonic's for the beam parameters used in our experiment (beam radius $r_b = 2.5$ mm is small compared to the wiggler radius $r_w = 2.5$ cm) one expects the effect of this resonance to be less dramatic than the gyroresonance. The figure 2-12 b) presents a plot of FEL output power scanned in B_z. As one can see from this figure there is a significant loss of efficiency for fields at and about the resonance field value (this was first seen by M.E. Conde [16]). But the interaction is not destroyed completely. This makes this regime, referred to as **antiresonance**, especially attractive for the study of unstable, possibly chaotic particle motion. C. Chen and R. Davidson [22] claimed that there is a possibility that for sufficiently high magnetic fields electron orbits exhibit chaotic motion at and near such resonances.

2.1.2 Space charge effects

As the ponderomotive potential (combined action of the wiggler field and the B-field of the electromagnetic wave) acts to bunch the electrons, the space-charge forces of the electrons counteract it. Depending on the density of the electron beam and the wiggler field strength these space-charge effects are more or less important. To quantitatively describe the effect of space charge let us once again consider the FEL dispersion relation (1.3). It can be rewritten in a form

$$(k - k_{em})(k - k_-)(k - k_+) = -\alpha^2 \tag{2.8}$$

where

$$\alpha^2 = F(\omega_b^2/c^2/2\gamma_0)\beta_w^2\beta_{z0}^{-2}k_w \tag{2.9}$$

is the coupling coefficient,

$$k_{em} = \left(\omega^2 - F\omega_b^2/\gamma_0\right)^{1/2}/c \tag{2.10}$$

is the electromagnetic mode wavenumber, and

$$k_\pm = [\omega - (v_{z0}k_w \pm P_1^{1/2}\omega_b/(\gamma_z\sqrt{\gamma_0}))]/v_{z0} \tag{2.11}$$

is the wavenumber of the space-charge shifted beam ponderomotive wave. We can now distinguish two high-gain operating regimes of the FEL referred to as the high-gain Compton (weak space-charge) and Raman (collective, strong space-charge) regimes.

High-gain Compton regime

In this regime the force on the electrons due to the ponderomotive potential dominates that due to the collective space-charge effects, and the gain length is shorter than the distance for a beam space-charge wave oscillation. In this limit the dispersion relation (2.8) reduces to

$$(k - k_{em})[k - (\omega/v_{z0} - k_w)]^2 = -\alpha^2, \tag{2.12}$$

where the space-charge term $P_1^{1/2}\omega_b/(\gamma_z\sqrt{\gamma_0})$ has been neglected. The maximum spatial growth rate occurs when k_{em} is equal to $(\omega/v_{z0} - k_w)$, reminiscent of equation (1.2). If, for a given set of FEL parameters, the beam current and energy were varied the real and imaginary parts of the roots of the dispersion equation would vary as well. The change in the $k_\pm$ is most crucial. It effectively determines whether there will be growth at all. Thus, even very high relative variation of beam density would not affect the roots of the dispersion (2.12) if the density remained small. A variation in energy, though, would drastically change the coefficients in the dispersion relation and hence its roots. To be able to neglect the space-charge term in the dispersion

relation (2.12) it is necessary to satisfy the following inequality [2]

$$\beta_w \gg \beta_{crit} \equiv F^{-1/2}(2P_1\omega_b c^2/v_{z0}^3\gamma_z^3\sqrt{\gamma_0}k_w)^{1/2}. \tag{2.13}$$

In the Compton regime the growth rate and the phase shift depend strongly on the electron beam energy (v_{z0}) and weakly on electron beam density (current).

Raman regime

In this regime the growth length is less than the oscillation distance for the space charge wave and the beam-plasma frequency is sufficiently high that for a given set of parameters the electromagnetic wave couples to only one of the two beam space-charge waves. The dispersion relation describing the interaction between the space charge beam mode and electromagnetic wave is obtained from (2.8). For the most effective coupling to take place the phase velocity of the ponderomotive force has to be equal to the phase velocity of the slow space-charge wave of the electron beam. The effect of the fast beam mode on the coupling in the Raman regime is weak and therefore $(k-k_+)$ can be approximated by $(k_- - k_+) = 2P_1^{1/2}\omega_b/(\gamma_z\sqrt{\gamma_0}v_{z0})$ in (2.8). The resulting dispersion relation is

$$(k-k_{em})(k-k_-) = -\alpha^2\gamma_z\sqrt{\gamma_0}v_{z0}/2P_1^{1/2}\omega_b. \tag{2.14}$$

It is necessary that

$$\beta_w \ll \beta_{crit} \tag{2.15}$$

for equation (2.14) to be a good approximation to the equation (2.8). Here one sees that the space-charge wave cannot be neglected. In the Raman regime the growth rate and the phase shift depend both on the electron beam energy (v_{z0}) and on electron beam density (that is the current or the plasma frequency, ω_b).

Our FEL operates in both Raman (Group II and the Reversed Field regimes which are mainly Raman) and the Compton regime (for the Group I mode of operation) regimes.

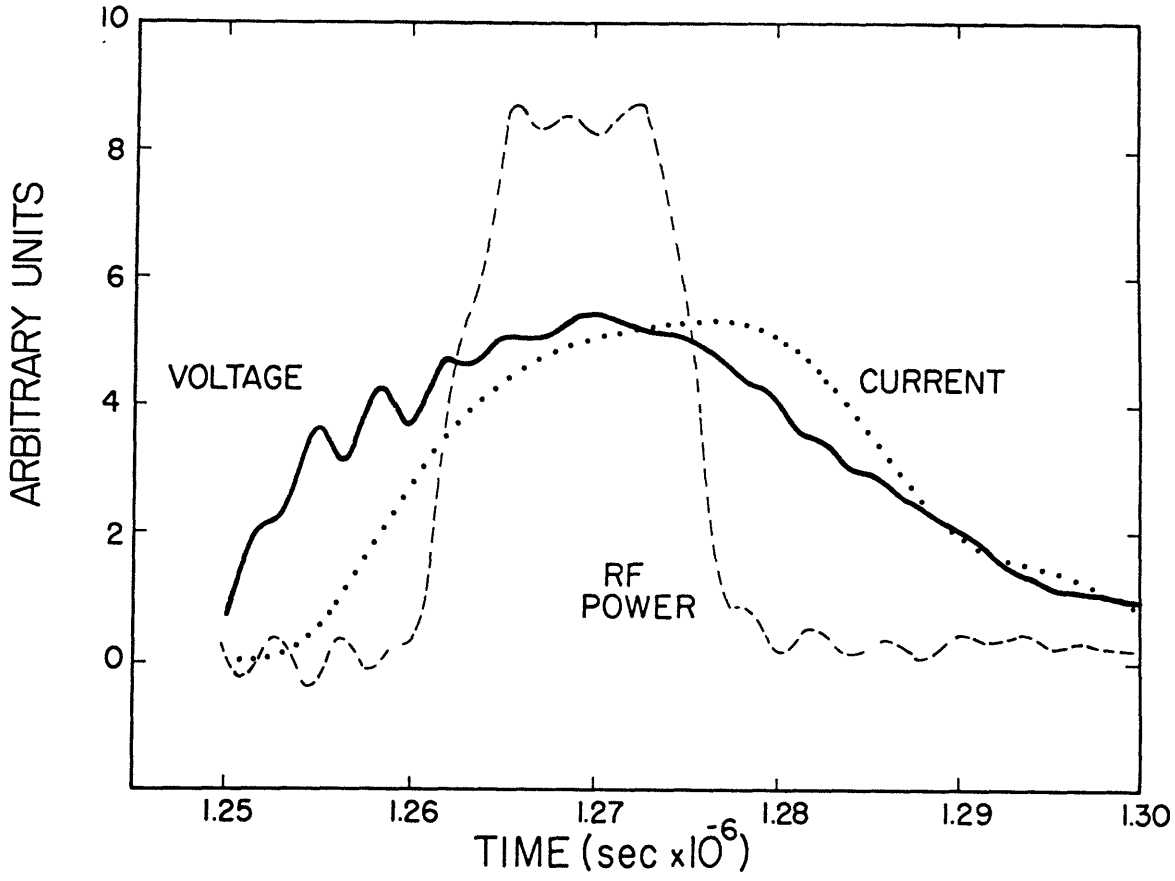

Figure 2-2: The measured beam current and voltage overlaid with an r.f. power-pulse, timed within 2 nsec, arbitrary units.

2.1.3 Chirping

If the phase shift $\Delta\phi$ of the amplified TE_{11} waveguide mode depends on time, it produces a change in frequency ($\delta\omega = \frac{\partial\Delta\phi}{\partial t}$). And indeed, in reality, in a pulsed system there will always be variations in the beam energy and current that would cause frequency changes. In our case both beam energy and current change appreciably over the length of the radiation pulse (see figure 2-2) . This effect is studied experimentally in this thesis. The derivation of the phase shift and frequency changes in a FEL amplifier was done by G. Shvets and J. Wurtele [23]. The linear theory presented there allows one to calculate the frequency changes explicitly.

To illustrate how a change in a parameter of a dispersive system can lead to

temporal phase variation and therefore to changes in frequency let us consider the example of dielectric beam loading. When the FEL interaction is absent the dispersion relation for the radiation pulse propagating in a waveguide is changed by the presence of the beam. This effect is of the same nature as the change of the refractive index when a wave propagates in a plasma. It seems natural that a plasma should increase the cut-off frequency of a waveguide. An easy derivation gives ${\omega_{c.o.}}^2{}_{eff.} = \omega_{c.o}^2 + p{\omega_p}^2$, where p is a factor less than unity that depends on geometry. The change in the index of refraction of a radiation of frequency ω in this case is

$$\delta n = \frac{c}{\omega}((\omega^2 - \omega_{c.o.eff.}^2)^{\frac{1}{2}} - (\omega^2 - \omega_{c.o.}^2)^{\frac{1}{2}}). \tag{2.16}$$

For small beam densities the change in the index of refraction is proportional to ${\omega_p}^2$. This effect is referred to as the beam loading.

Now imagine an electron beam that is moving to the right with a density increasing towards its tail. At the head of the pulse, the peaks of the EM wave have a phase velocity slower than those further back (due to the beam loading). This results in peaks at the tail catching up with peaks at the head, and, therefore, in a frequency upshift (see figure 2-3 where a radiation pulse envelope is laid over the beam density profile as they propagate together along the z-axis).

The FEL interaction results in a more complex dependence of the index of refraction on the FEL parameters as one can infer from the form of the dispersion relation (1.3). Variations in current and energy produce shifts in the detuning from FEL resonance and in the beam-wave coupling. It is shown in reference [23] that it is primarily detuning that determines the frequency evolution and, thus, in the Raman regime, the frequency is sensitive to both current and energy, while in the Compton regime the frequency changes depend mostly on the change in the beam energy.

The Raman FEL interaction produces a downshift with the *same* moving density gradient shown in figure 2-3. The radiation couples to the slow space-charge wave, whose phase velocity becomes slower as the beam density increases. Adjacent radiation peaks now move farther apart with increasing interaction distance, and the

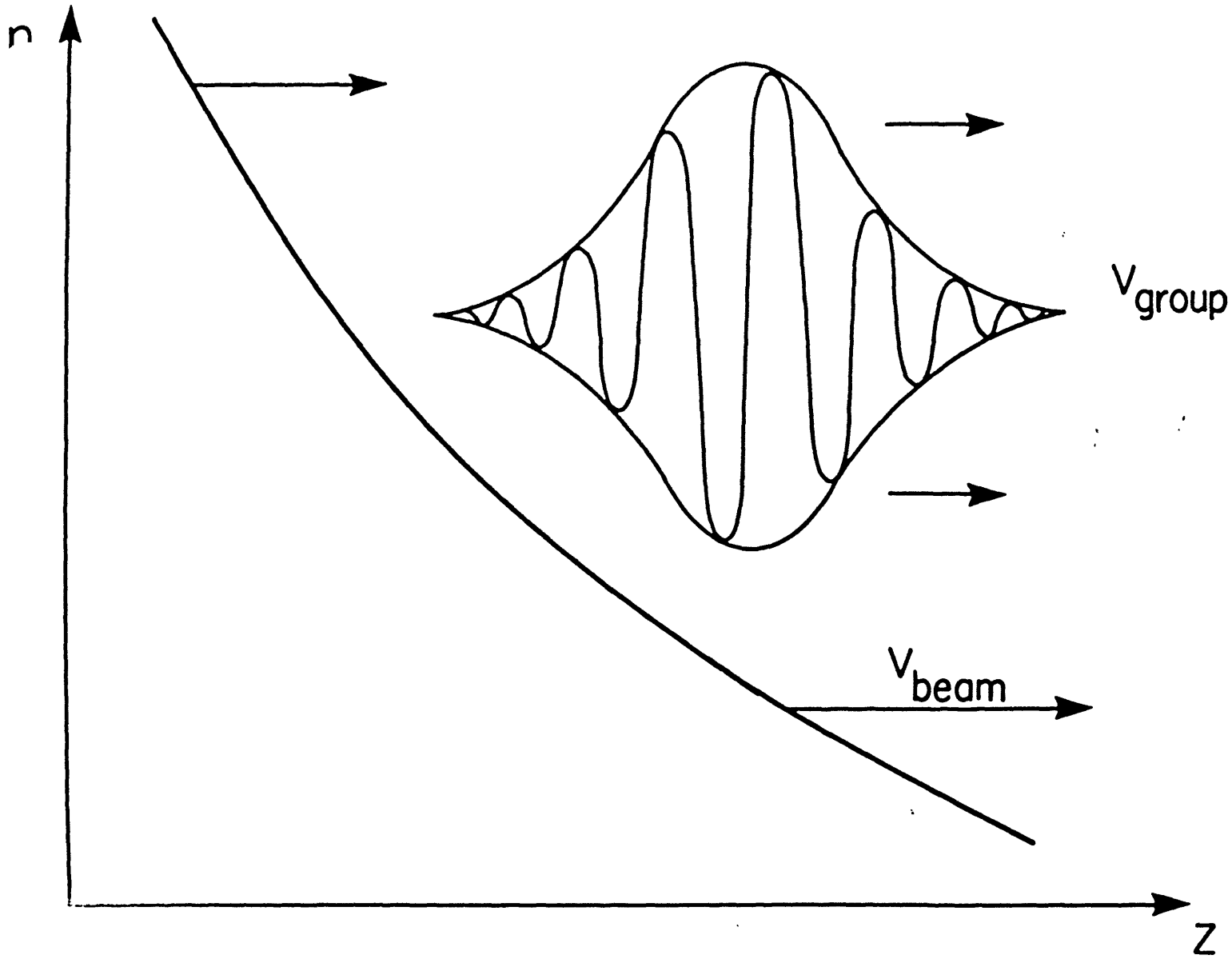

Figure 2-3:

frequency downshifts. For a Compton FEL, the only resonant contribution to phase shift comes from the energy variation. Yet in the Raman regime resonant contributions to the phase shift come from both current and energy variations. As shown in [23] if the slope of the current and the energy variation both have the same sign, the resulting frequency shifts will have opposite signs and will tend to cancel.

2.2 Experiment

The amplified microwave radiation from the FEL is dumped into an "anechoic" (reflection free) chamber via a conical horn as shown in figure 1-1. A small fraction (approximately 30 dB down in power) of this radiation is collected by a receiving waveguide on the opposite side of the box. The radiation collected by this receiving waveguide is then measured with the view of determining the total output power level and the time history of the phase shift of this FEL system.

Power measurement

The power level is determined from the response of a calibrated crystal detector (HP R422A). The radiation that enters the receiving WR-28 waveguide goes through calibrated fixed attenuators, a variable attenuator, a sharply ramped band-pass filter (1.7 GHz full width at 3 dB points) and is finally rectified by the crystal detector. The precision calibration of all the microwave components was done using a network analyzer. The attenuation in the air gap between the horn and the receiving waveguide, necessary for determining the absolute power output of the FEL was measured by a substitution method by Conde [7].

The kicker magnet is used to change the length the electron beam is allowed to interact with the radiation before it is deflected into the drift tube's wall. This magnet produces strong transverse magnetic field (approximately 1 kG). It serves as an important tool in measuring the power, phase shift, and chirping of the FEL as a function of interaction length.

Phase measurements using a Double Balanced Mixer

The phase shift was measured using an interferometric technique. A hybrid-T junction served as the interferometer. The attenuated FEL output was the test signal. A fraction of the microwave power from the magnetron, used to drive the FEL, was tapped to provide the reference signal (see figure 2-4).

The *hybrid-T* junction is a common piece of microwave hardware which is discussed in most reference books on microwave engineering [24]. The device is illustrated in figure 2-4. The signal from an input arm (either the reference or the test arm) is

split evenly between the two output arms but cannot couple to the other input arm since the electric fields in the input arms are cross-polarized with respect to each other. The signal from the input which has its E-field plane perpendicular to the E-field plane of the output arms splits evenly but is 180^o out of phase into the two output arms. The signal from the other input arm (E-field parallel to the output arms E-field) splits evenly and in phase into the two arms. The electric fields in the two output arms add:

$$E_{o,1} = E_{i,1}sin(\omega t + \phi_1) + E_{i,2}sin(\omega t + \phi_2), \tag{2.17}$$

$$E_{o,2} = E_{i,1}sin(\omega t + \phi_1) + E_{i,2}sin(\omega t + \phi_2 + \pi), \tag{2.18}$$

where $E_{i(o),j}$ is the field in the jth input (output) arm. The power flow in each arm can be calculated from the time averaged square of the electric field. The power in each output arm is

$$P_{o,1} = C_p\frac{1}{2}[{E_{i,1}}^2 + {E_{i,2}}^2 + 2E_{i,1}E_{i,2}cos(\phi_1 - \phi_2)] \tag{2.19}$$

$$P_{o,2} = C_p\frac{1}{2}[{E_{i,1}}^2 + {E_{i,2}}^2 - 2E_{i,1}E_{i,2}cos(\phi_1 - \phi_2)] \tag{2.20}$$

where C_p is a dimensional factor that relates power to field value for the lowest $TE_{1,0}$ mode of the WR-28 waveguide.

Difference between the power in the output arm 1 from the power in the output arm 2 depends on the relative phase difference between the two input signals:

$$\Delta P = C_p 2E_{i,1}E_{i,2}cos(\phi_1 - \phi_2). \tag{2.21}$$

The setup

If the phase measurement is desired, the radiation collected by the receiving waveguide passes through a 1.7 GHz wide band pass filter, a phase shifter, and into a hybrid T junction.

The reference magnetron signal ($\sim$ 500 ns FWHM) is delayed such that the FEL

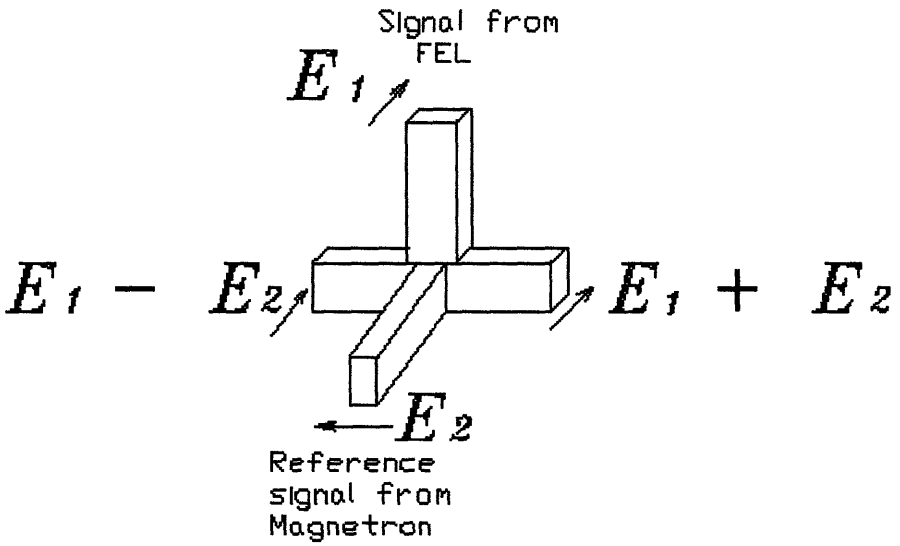

Figure 2-4: A hybrid T device. The arrows indicate the direction of electric fields in the lowest $TE_{1,0}$ mode.

output is mixed with the 18 ns portion of the magnetron pulse that was amplified. The phase of the magnetron radiation fluctuates throughout the 500 ns wide pulse. The measured shifts are not affected by the fluctuations of the phase of the magnetron radiation throughout the 500 ns wide pulse, because when the delay is in effect the phase in the reference signal is exactly the same as the phase in the FEL signal at interaction length $z = 0$ m.

For maximum sensitivity, the two microwave pulses are tuned by variable attenuators to be approximately equal in amplitude. The resultant output powers from the hybrid T are measured by calibrated crystal detectors. In order to minimize reflections from the crystal detectors and hence the mismatch in the T (when powers from the input arms are split unevenly) two 10 dB couplers are placed between the detectors and the hybrid T output arms.

From equation (2.21) the difference between the signals from the two detectors is proportional to the product of the cosine of the phase shift and the field amplitudes in the input arms. In order to remove the dependence on the field amplitudes (they may vary in time) in the input arms we measure the four power pulse-shapes, $P_{o,1}, P_{o,2}, P_{i,1}, P_{i,2}$, and construct a quantity $\frac{P_{o,1}P_{o,2}}{\sqrt{P_{i,1}P_{i,2}}}$ that is proportional to the cosine of the phase shift only.

At each phase shifter setting, three FEL shots are fired and $P_{o,1}, P_{o,2}, P_{i,1}, P_{i,2}$ recorded on oscilloscopes. The phase shifter is then advanced by 60^o and the above measurements repeated. The resolution of the oscilloscopes allows us to take data for about 18 time positions in a pulse, separated by 1 ns intervals. After six successive settings of the phase shifter the data at each time position is fitted by a least squares method to a sinusoid. An example of a sinusoidal fit for a certain time in the pulse is shown in figure 2-5. The same procedure is performed with the electron beam turned off. The phase shift in the FEL is determined for each time position from the phase difference between the two sinusoids.

A total of 18 shots are necessary for a single phase measurement. The phase is recorded as a function of time in the pulse and the interaction distance (z) down the drift tube. This removes the $2\pi n$ ambiguity (where n is an integer), because we know that for the case of zero interaction length, (or no beam), the phase shift is zero and that the phase changes continuously with the interaction distance.

2.3 Results

In this section the results of the intensity and phase shift measurements of the FEL system are presented. We compare power output, phase and more importantly frequency shifts (they are proportional to the temporal derivative of the phase shifts) accumulated in the three basic regimes of operation of the FEL (see the previous section): Groups I and II, and the Reversed field regime. A comparison with the theoretical predictions and the computer simulation results is made. This section also contains results of the measurements in the anomalous 'Antiresonance' regime.

2.3.1 Intensity measurements

The output power was measured as a function of the length of the interaction region. Figures 2-8 b), 2-9 b), and 2-10 b) show the result of this measurement for the three different regimes.

The small signal growth is the highest in Group I (44 dB/m) but the power level

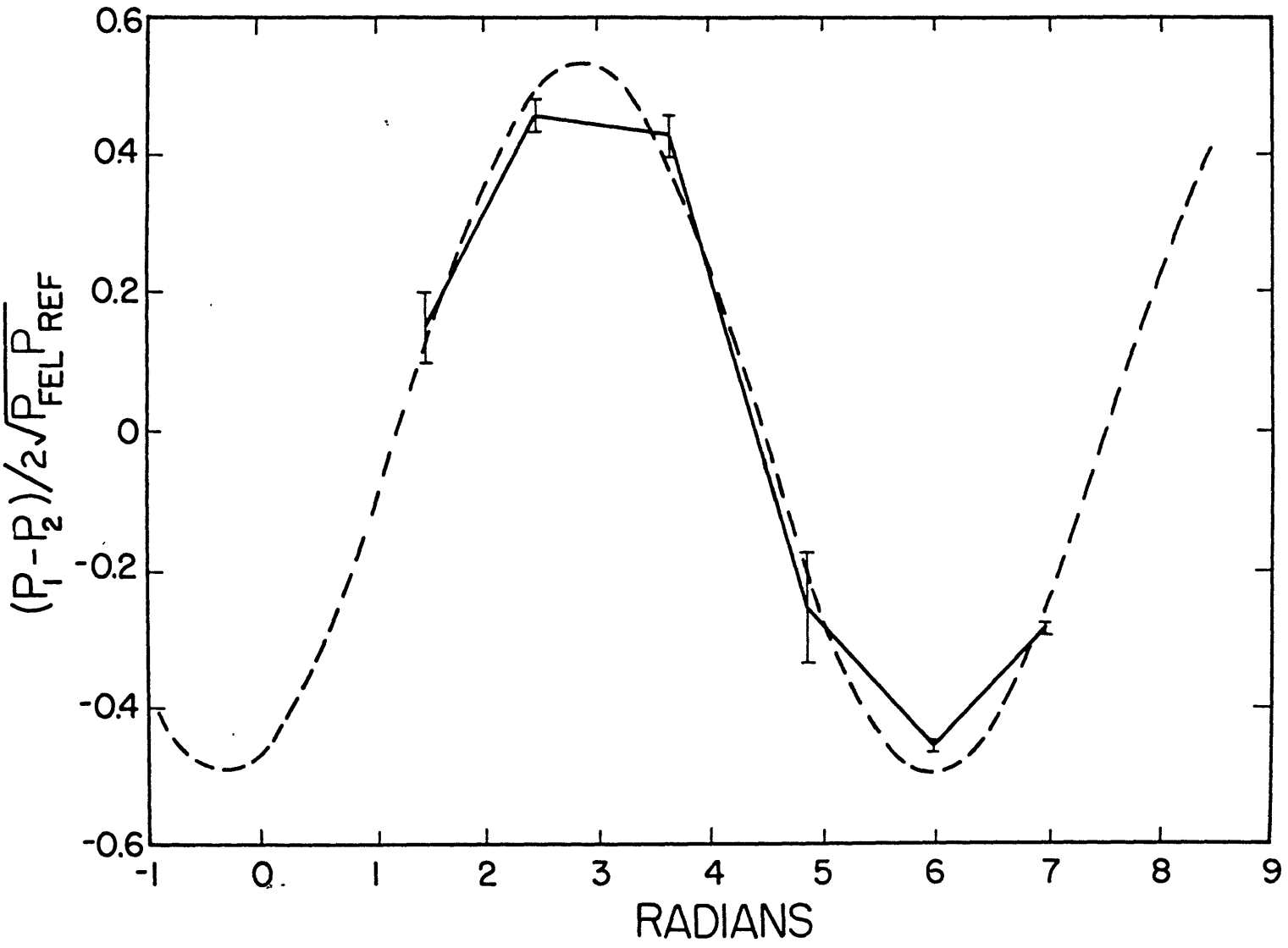

Figure 2-5: An example of a sinusoidal fit to determine phase at a certain time in the pulse.

reaches saturation with an efficiency (the percentage of the beam power beam voltage times beam current, converted into the radiation power) of $\sim$ 9%. Operation in Group II shows the lowest growth rate and the lowest efficiency of $\sim$ 5%. The Reversed Field regime has a by far the highest efficiency (27%) with the highest power level of 61 MW.

2.3.2 Phase in the three Regimes

Figure 2-6 shows the temporal behavior of the FEL phase shift $\Delta\phi(t)$ in all three regimes for 15 descrete times during the voltage pulse. The data shown corresponds to the central fifteen nanoseconds of approximately 15 ns (FWHM) wide radiation pulses like the one in figure 2-2. The measurements shown were taken for an interaction length z of approximately 160 cm. Similar measurements were made for a wide series of interaction lengths.

We see that the largest phase changes occur in the Group I regime of operation, and that there is a very pronounced phase upshift followed by a strong phase downshift. The largest variations take place as the beam voltage first ramps up and then ramps down as expected. In Group II and the Reversed field regimes the phase changes are seen to be relatively small.

2.3.3 Frequency shift

The temporal history of $\Delta\phi(t)$ allows one to determine the instantaneous frequency shift from the relation

$$\Delta f = \frac{1}{2\pi}\frac{\partial\Delta\phi(t)}{\partial t}. \tag{2.22}$$

The results are illustrated in the figure 2-7 as a function of interaction length z for all three regimes of FEL operation. The data were obtained from equation (2.22) and measurements like those shown in figure 2-5. In the case of Group I we show the *maximum* measured frequency upshifting, early in the pulse, followed by maximum frequency downshifting that occurs later in the pulse. The frequency gradients

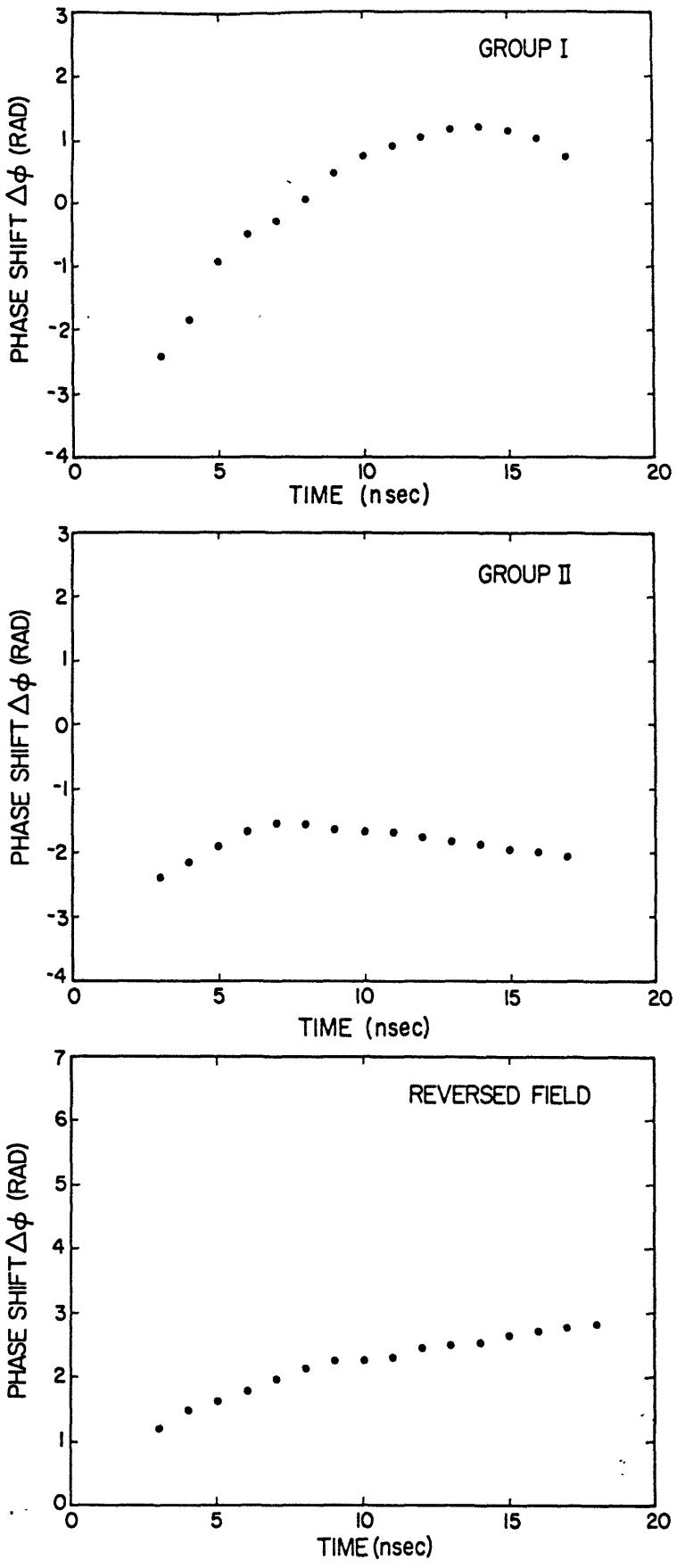

Figure 2-6: The phase shift at 15 discrete times in a pulse in the Group I, Group II and Reversed Field regimes.

as function of interaction length are respectively, $\partial\Delta f/\partial z = +50$ MHz/meter and $\partial\Delta f/\partial z = -32$ MHz/meter length of interaction region. Note that the frequency shift changes inside the pulse, which is often referred to as *chirping.*

In the Group II regime the chirping is considerably less than that in the previous case and the maximum upshift and downshift are $\partial\Delta f/\partial z = +23$ MHz/meter and $\partial\Delta f/\partial z = -8.6$ MHz/meter.

In the Reversed Field regime the phase increases almost linearly with time so that Δf is nearly constant over the duration of the pulse. One finds that $\partial\Delta f/\partial z = +8$ MHz/meter.

The strong observed frequency shifting in Group I and the much weaker effect in the other two regimes is consistent with earlier spectroscopic measurements [25]. In the latter, frequency shifting (about 100 MHz) was seen only in Group I; in the remaining two regimes the sensitivity, unlike in the present studies, was too poor to resolve any frequency changes.

2.3.4 Comparison with theoretical and numerical results

The fact that shifts in Group I (closer to Compton regime) are larger than those in Group II and Reversed field regimes (mainly Raman) is consistent with the argument [23] that in the Compton FEL it is the energy (beam voltage) that affects the phase the most, while in the Raman regime the detuning contains an equally large contribution from the current, whose effect however is to counteract the phase change caused by electron energy variations.

A comparison of data with the predictions of a numerical code WTDI [8] has been made. This is a time independent, three-dimensional, nonlinear, slow time-scale amplifier code which assumes a single waveguide mode (in our case the $TE_{1,1}$ mode of a circular waveguide). The code also takes into account the dispersion characteristics of the right (left) circularly polarized wave on the electron beam (i.e. dielectric beam loading), and models, in an approximate way, for a.c. space charge effects from the bunched beam. Space-charge effects are important in our FEL, since they affect the magnitude of the detuning in the Raman regime and the saturation power.

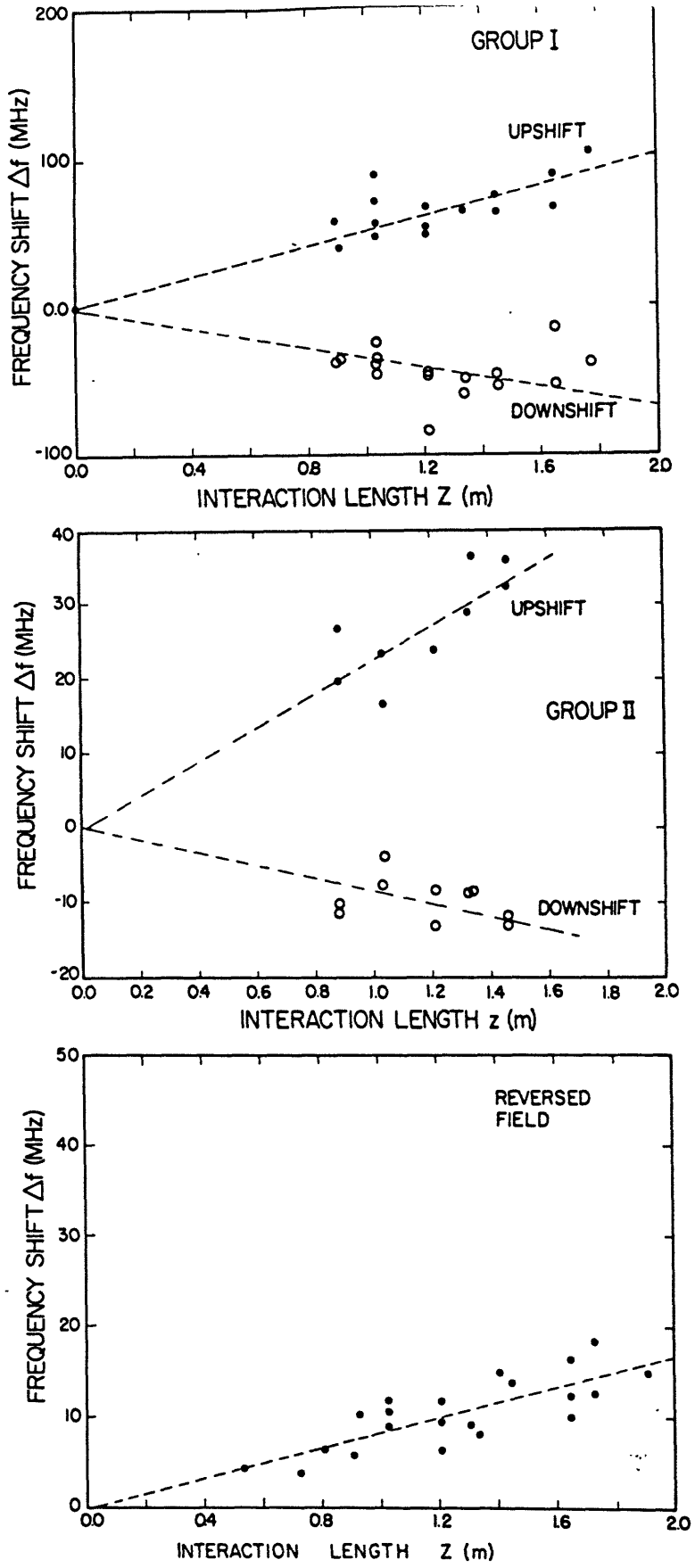

Figure 2-7: Frequency shift vs. interaction length. The dashed lines represent linear fits to the experimental results.

Figure 2-8 illustrates the results for operation in the Group I regime. The lower graph shows the peak measured r.f. power during the pulse. The upper diagram gives the phase at two separate instances of time in the pulse; early in the pulse at t=2 ns where the beam energy is well below its maximum value (see figure 2-2), and later in the pulse at t=22 ns, past the maximum in the beam energy. This illustrates the great sensitivity of the phase to the instantaneous value of the beam energy. The solid lines represent simulations using parameters of table 1.2. The agreement between measurements and simulations is at best fair.

Figure 2-9 shows experimental and numerical results in the Group II regime. The r.f. power shown is again the maximum measured during the pulse.

Figure 2-10 gives results for the Reversed Field regime. The simulations are for the parameters listed in Table 1.2 . The agreement with measurements is fair. However, parameter modification in the simulations such as in emittance ϵ_n and/or in the beam energy γ can lead to vast improvements in the agreement between experiment and theory. We illustrate this fact in figure 2-11 in which the normalized emittance was taken to be 0.8×10^{-2} cm-rad instead of 2.3×10^{-2} cm-rad as given in Table 1.

As pointed out above, the WTDI code is time independent and is thus, in general, unable to give information about chirping. However analytical calculations [23] show that the measured chirping is in qualitative agreement with theory. Since the group velocity of the waveguide mode is, for our parameters, near the axial beam velocity, the phase shift at each point in time, calculated with the assumption of steady state operation, can be used to estimate the chirping.

2.3.5 Antiresonance

At the Antiresonance the r.f. power level drops precipitously as is seen in figure 2-12 . Here any erratic behavior of Δf may possibly be used as a signature of unstable FEL operation. Such may be due to current or voltage fluctuations or due to chaotic particle orbits [22]. Figure 2-13 a illustrates the lack of the reproducibility of Δf on a series of successive shots. This is to be compared to the good reproducibility of measurements taken in a FEL parameter range slightly removed from the precise po-

sition of the antiresonance, shown in figure 2-13 b. We note that such measurements are not possible at gyroresonance because there the instability is so strong as to drive the electrons into the waveguide walls, thereby terminating the FEL interaction.

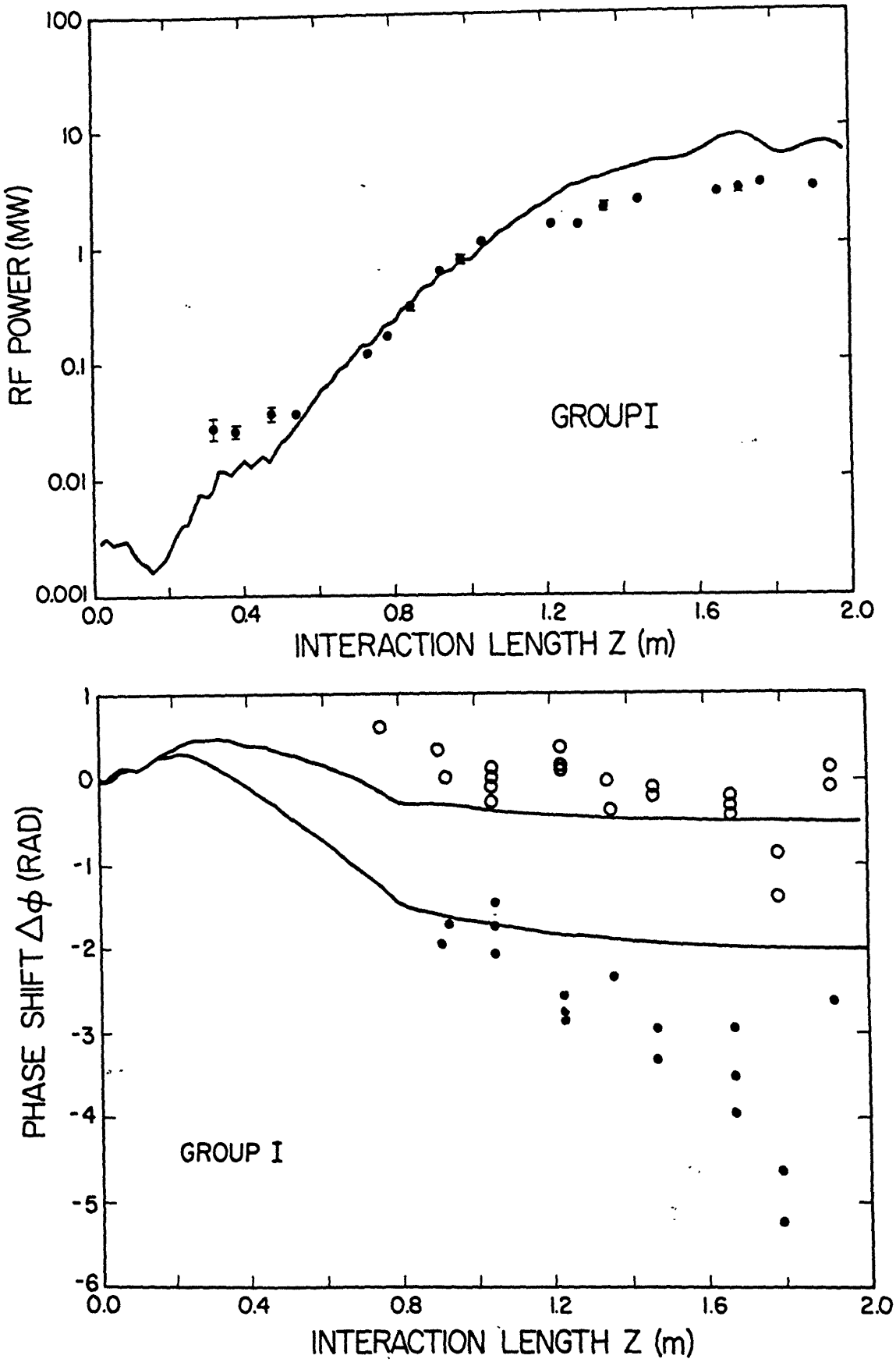

Figure 2-8: Group I regime. Comparison of the simulation results (shown as lines) and experimental data (symbols).

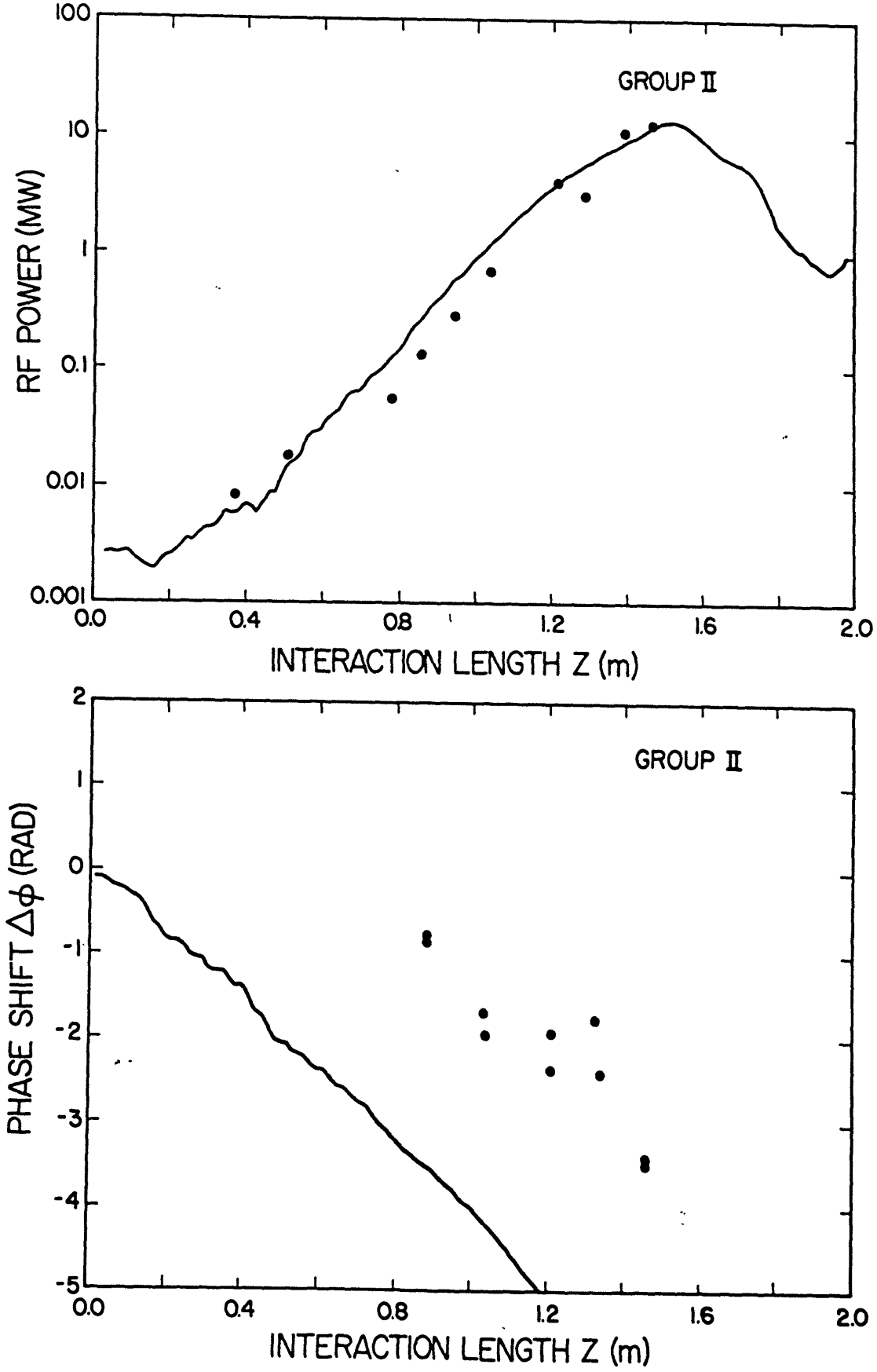

Figure 2-9: Group II regime. Comparison of the simulation results (shown as lines) and experimental data (symbols).

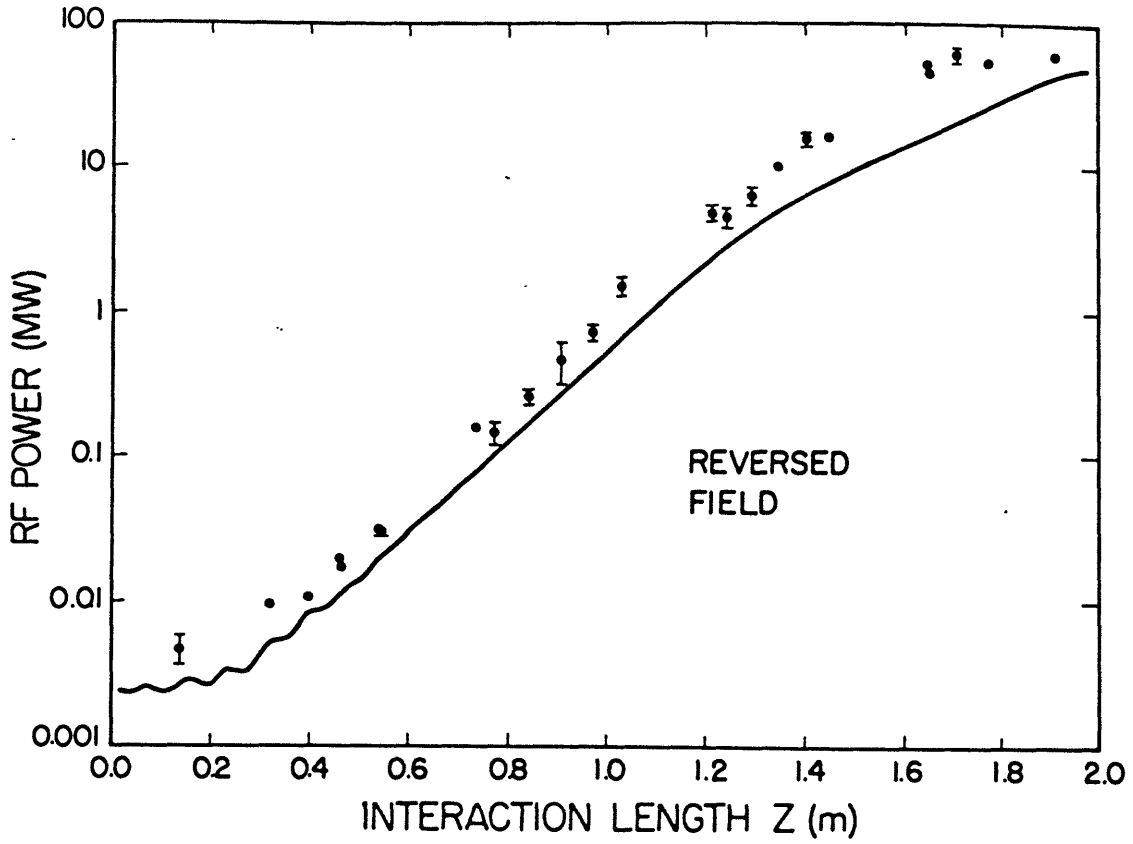

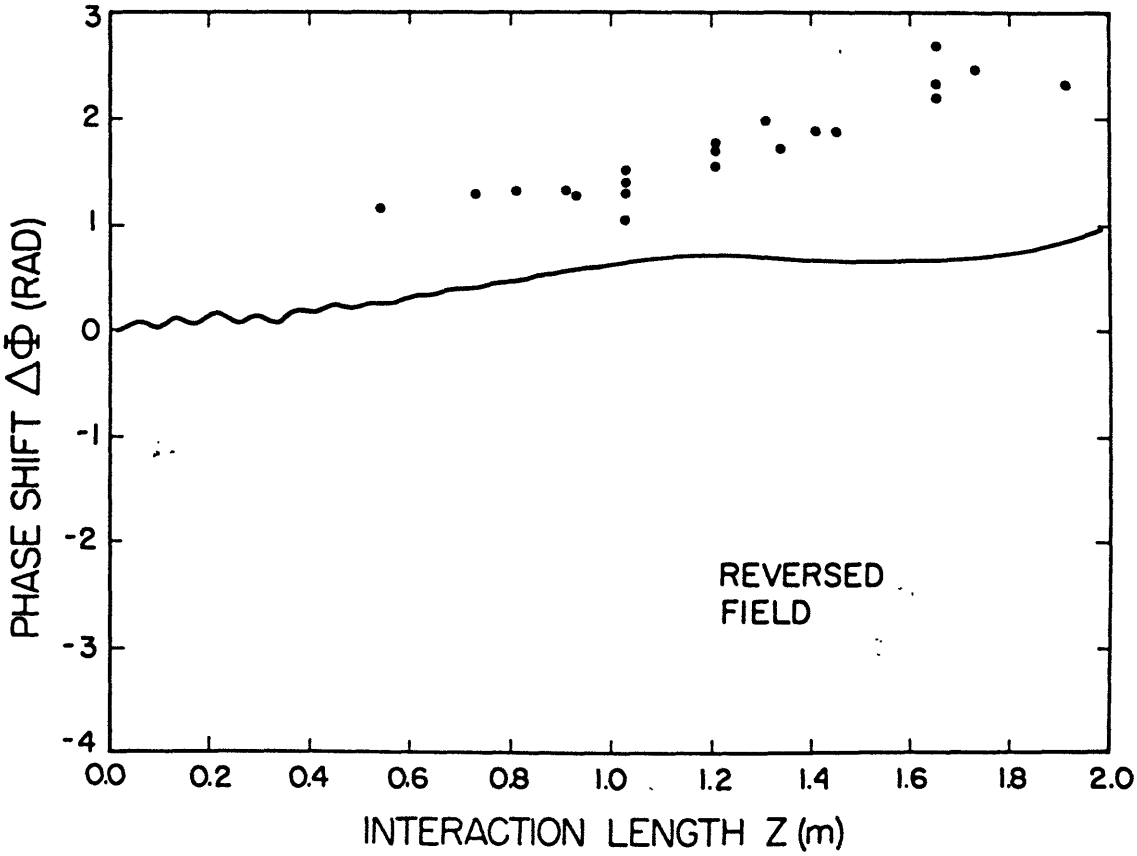

Figure 2-10: Reversed Field regime. Comparison of the simulation results (shown as lines) and experimental data (symbols).

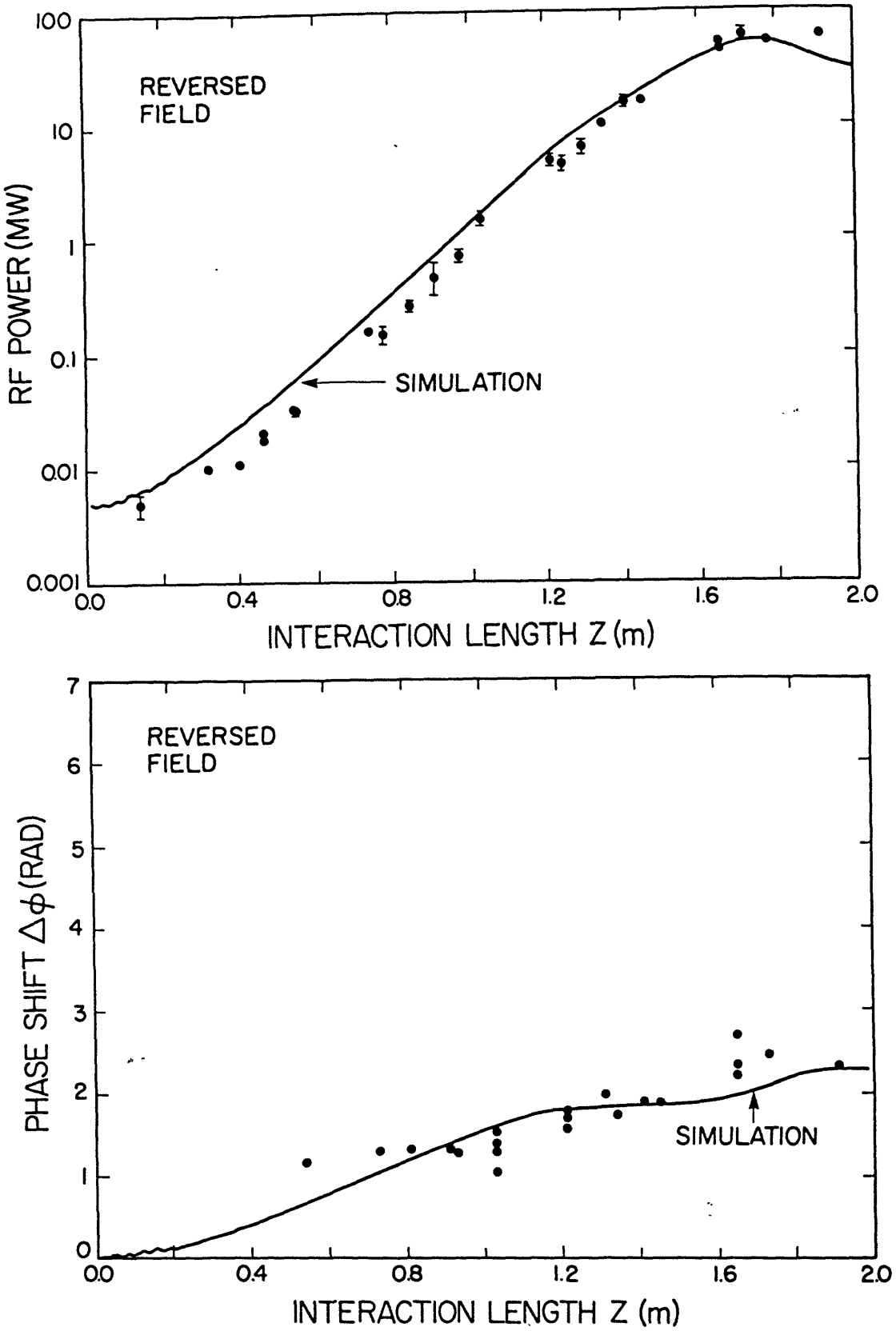

Figure 2-11: Reversed Field regime. Comparison of the simulation results with beam's emittance input parameter changed to achieve better agreement (shown as lines) and experimental data (symbols).

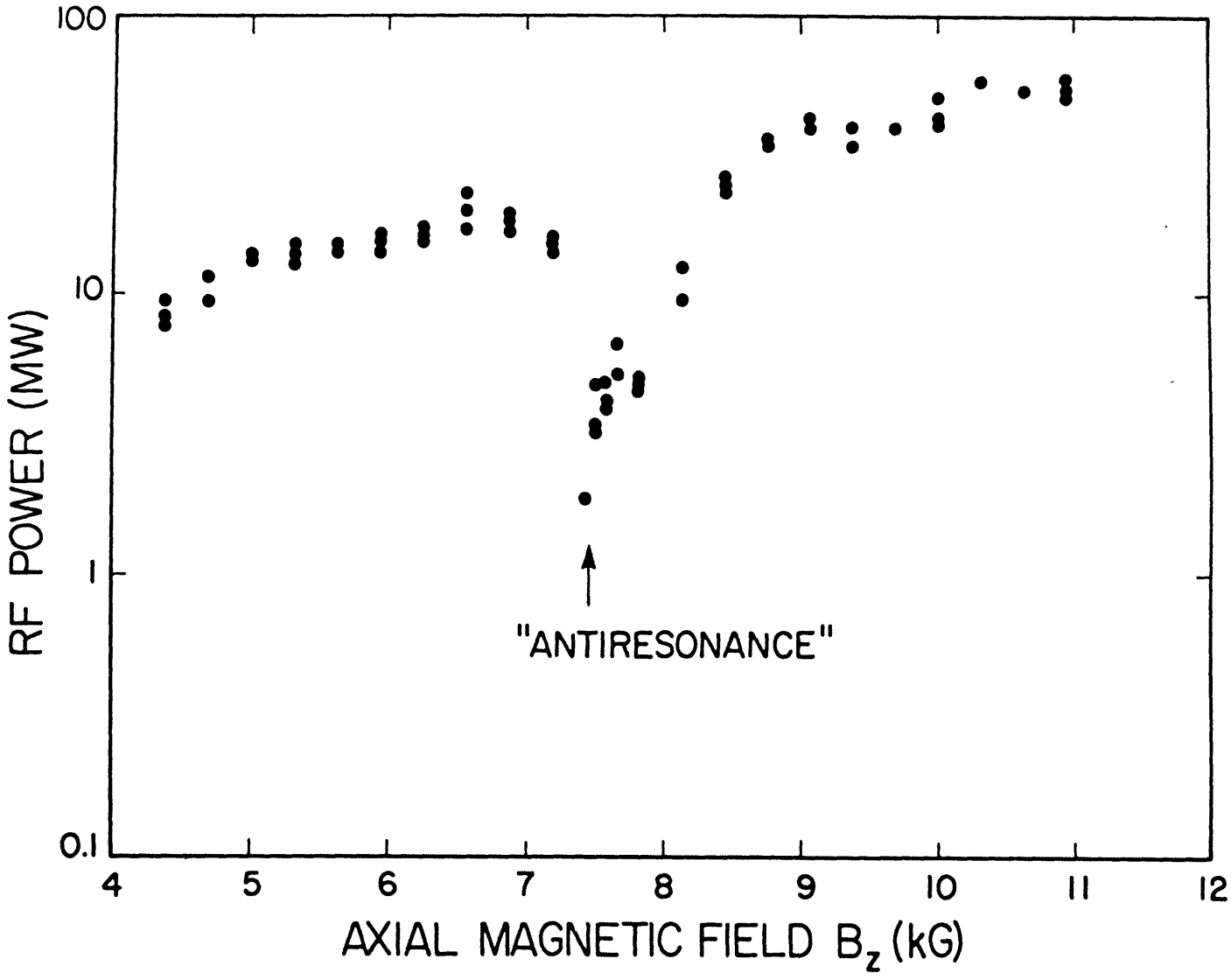

Figure 2-12: Power vs. guiding field at antiresonance.

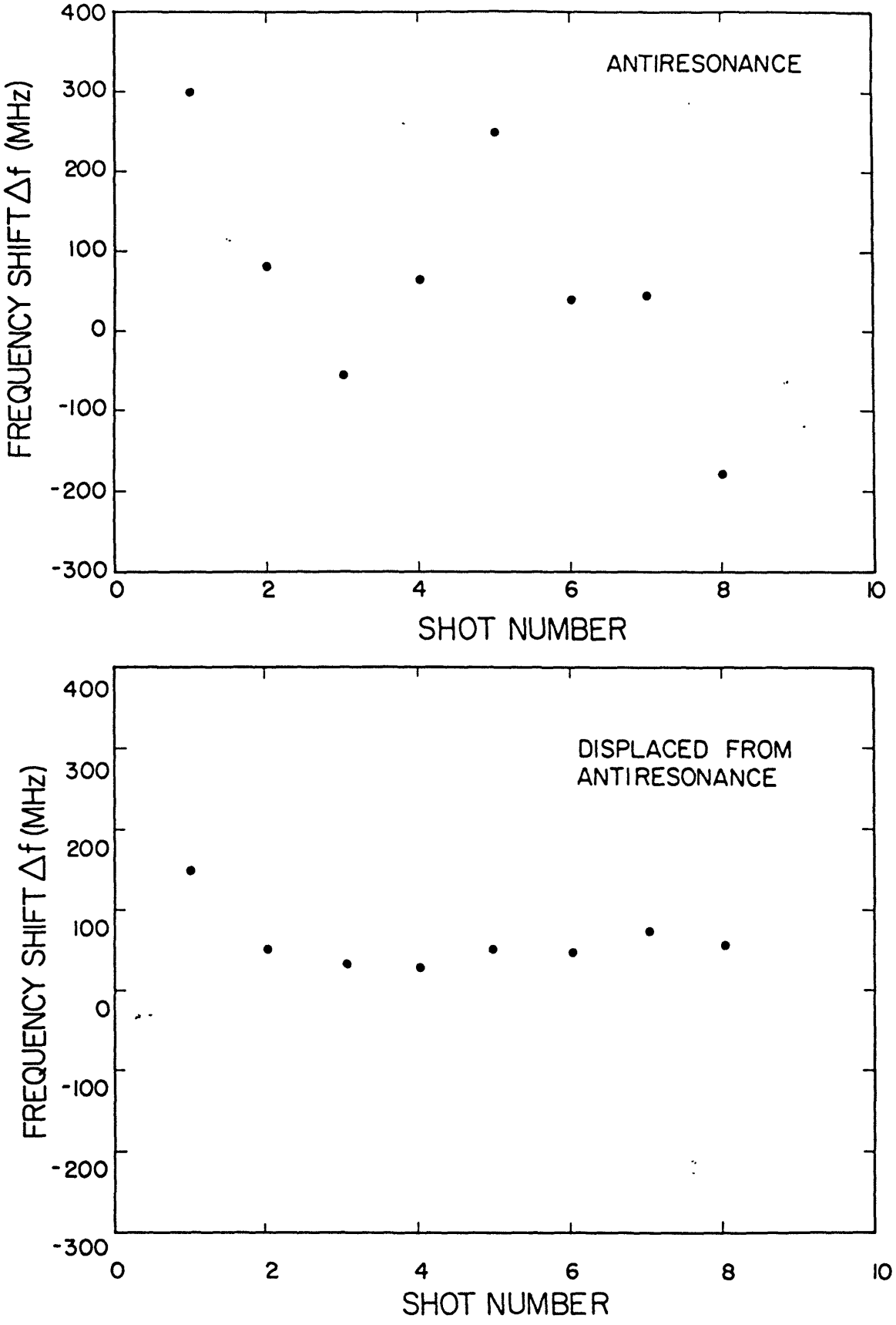

Figure 2-13: a) Successive measurements of the frequency shift at Antiresonance, $B_g = 7.47$ kG. b)Successive measurements of the frequency shift with $B_g = 8.4$ kG.

Chapter 3

HGA

The two-beam accelerator [26] is a promising candidate for achieving the ultra-high electron energies (of the order of or higher than 1 TeV) required in the next-generation linear colliders.

The field gradient achievable in a r.f. accelerator is probably limited by electrical discharge breakdown-like processes. It has been argued [9] that the higher is the frequency of the driving radiation the higher will be the gradients that could be achieved without breakdown or other kinds of failure. That is one of the motivations for creating a High Gradient Accelerating (HGA) structure at such high frequency. The other is the reduced energy expenditure required to power a 1 TeV linac.

For driving the HGA we used the FEL described in Chapter 2 of this thesis. It produces 60 MW r.f. power, 18 ns long pulses. A high power magnetron is the input power source for the FEL amplifier. It essentially determines the tunability of the FEL. The operating frequency range of the magnetron is from 30 to 35 GHz. The frequency of the magnetron pulse is stable to within at least 5 MHz. However the frequency shift induced by the FEL interaction could be of some concern (see Chapter 2). In the FEL used in the tests the frequency shift is measured to be 16 MHz with 5 MHz scatter in the Reversed Field regime. The bandwidth of the HGA is greater than 500 MHz. Thus the MIT's FEL is acceptable for the purposes of the experiments described in this Chapter. For actual acceleration however, where the phase stability is of much greater importance, a phase stability better by one order of magnitude

(< 1 MHz) would be needed.

3.1 The HGA

The 32.98 GHz disc-loaded constant gradient traveling-wave accelerating structure (its photograph is shown in figure 1-2) was built as prototype of an element in the accelerating line of the two-beam CERN-CLIC accelerator. It is a $2\pi/3$ mode, $v_p = c$ constant gradient iris disc-loaded waveguide structure. It consists of 26 cells, each of 3.029 mm in length and 2 coupler cells 3.56 mm long. The total length of the structure is 0.08587 m. The fill time of the structure is 3.42 ns, with a group velocity of 0.083c. The two side-couplers are at right angles to the axis of the structure. They couple the power from a standard WR-28 rectangular waveguide into the desired mode of the structure. The high vacuum of around 1×10^{-7} Torr is maintained by two 30 liters/sec ion-pumps and two smaller auxilliary ion pumps with pumping speed of 2 liters/sec. The structure was designed to have shunt impedance of 116 MΩ/m. This means that for input power level of 60 MW the maximum accelerating gradient is approximately 110 MV/m. However the CERN-CLIC structure was designed for accelerating gradients of approximately 80 MV/m. Note that the r.f. fields at the metal discs are expected to be higher. Some of the key parameters of the HGA are shown in table 1.3.

3.2 Experimental Setup

3.2.1 Frequency Calibration of the FEL

The magnetron frequency was set to the desired value by mixing with a local oscillator. A small portion of the magnetron output was sampled by means of a directional coupler. Then, much like the phase measurements of the Chapter 2, it is "mixed" with the output of a Hewlett Packard 8690A Sweep Oscillator in a hybrid "T" junction (see figure 3-1). The oscillator frequency is determined by a Hewlett Packard 5353A Microwave Frequency Counter.

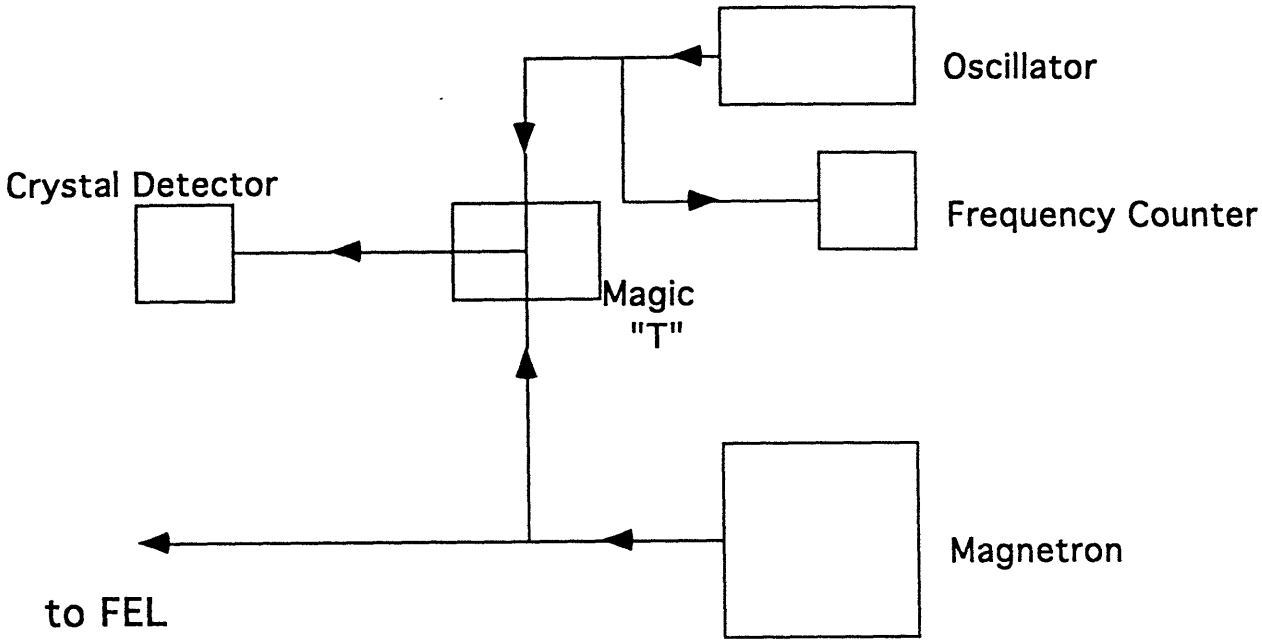

Figure 3-1: Schematic of the measurement setup for the magnetron frequency.

One of the side arms of the "T" is terminated in a matched load while the other ends in a crystal rectifier, the output of which is displayed on a Hewlett Packard 1 Gsample/sec 54510A Digitizing Oscilloscope. The beat waveform of the two signals (see equation (2.21))is displayed as the varying part of the oscilloscope pulse-shape. The duration of the magnetron pulse is close to 500 ns, so the frequency of the magnetron could in principle (were it not for the intrinsic phase jitter of the device) be set to within 2 MHz of the frequency of the Sweep Oscillator. An example of a beat signal with magnetron tuned to the frequency of the Sweep Oscillator is presented in figure 3-2.

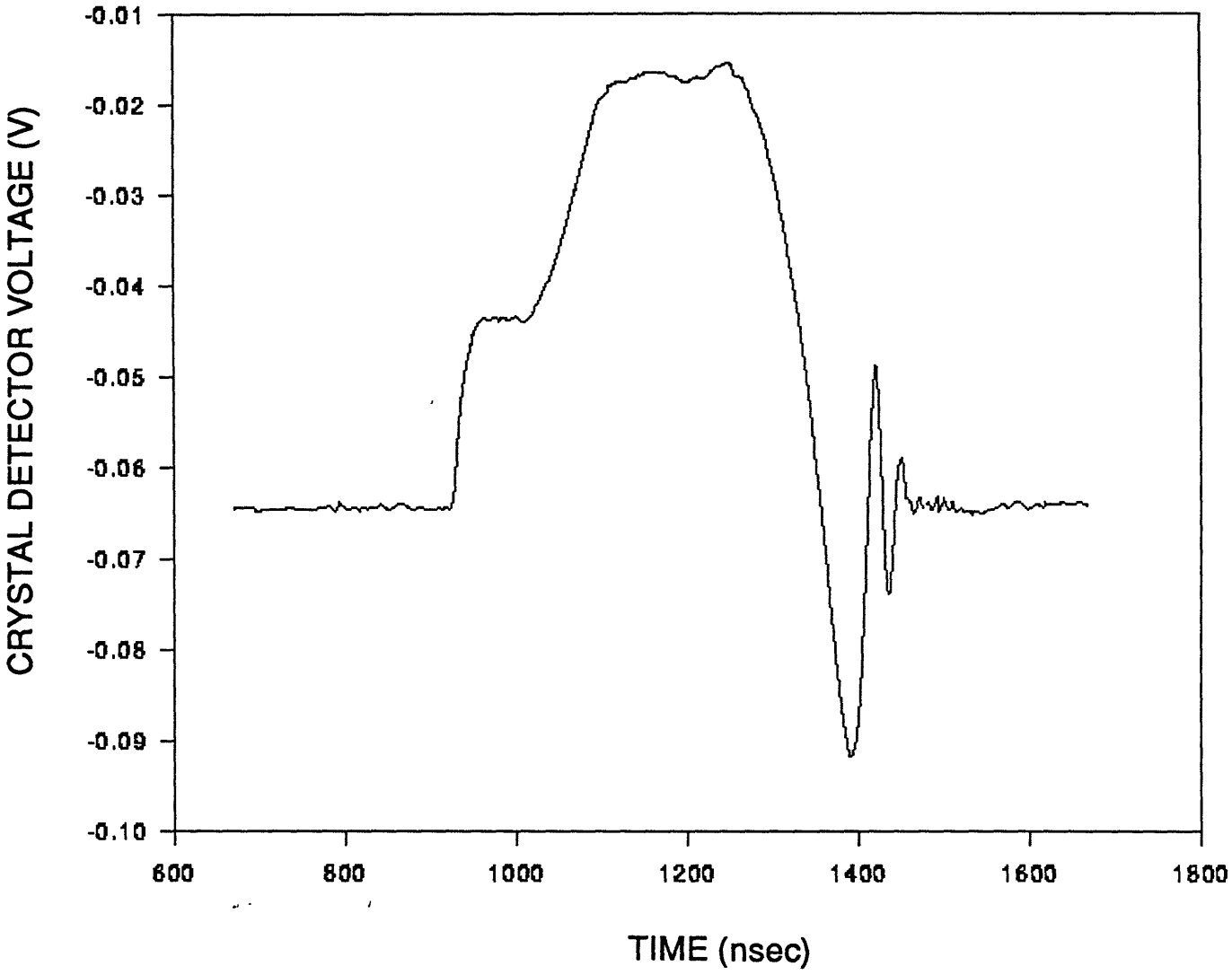

Figure 3-2: Example of the magnetron frequency measurement. The beat signal as function of time shows few oscillations when the magnetron is carefully tuned to the frequency of the local oscillator.

3.2.2 HGA Testing Apparatus

The schematic of the HGA testing apparatus is shown in figure 3-3. The amplified signal exits the FEL in $TE_{1,1}$ mode of a circular waveguide. It is then converted from circular polarization to linear polarization by means of mode converter. The converter is described in the next subsection. The adapter from circular to WR-28 rectangular waveguide then follows. The HGA operates under the high vacuum of around 1×10^{-7} Torr. It has to be separated from the relatively high pressure FEL and the horn dump section where the pressure is typically 10^{-5} to 10^{-6} Torr. Two ceramic windows are used to isolate the high and the low vacuum sections. As a preventative measure against high power breakdown on these windows the surface area of the windows is increased by gradually uptapering the WR-28 waveguide to WR-187, positioning the windows at this larger area, and downtapering the waveguides back to WR-28.

Input, reflected and transmitted power diagnostics are made available by placing high vacuum directional couplers made at CERN immediately before and after the HGA. Variable attenuators and calibrated crystal-detectors allow one to infer the absolute power levels. The entire system is calibrated absolutely using a network analyzer and by a substitution method, i.e. by measuring the received power in terms of the known input power.

3.2.3 Polarization Converter

The FEL microwave output is produced in a circularly polarized mode. In order to maximize the fraction of this power available for HGA testing, a high-power circular to linear polarization converter has been fabricated [27] and was employed. This converter is a section of circular waveguide, 4.0 inch long, 0.625 inch O.D., 0.550 inch I.D., squeezed over a 1-1/2 inch length to produce a slightly elliptical cross-section. Its design analysis is given in reference [28]. The squeeze-direction is at an angle of 45^o to the plane of electric field of the linearly polarized $TE^0_{1,1}$ mode produced at the end of the converter. The final O.D. at the narrow dimension of the squeezed section is 0.548 inch.

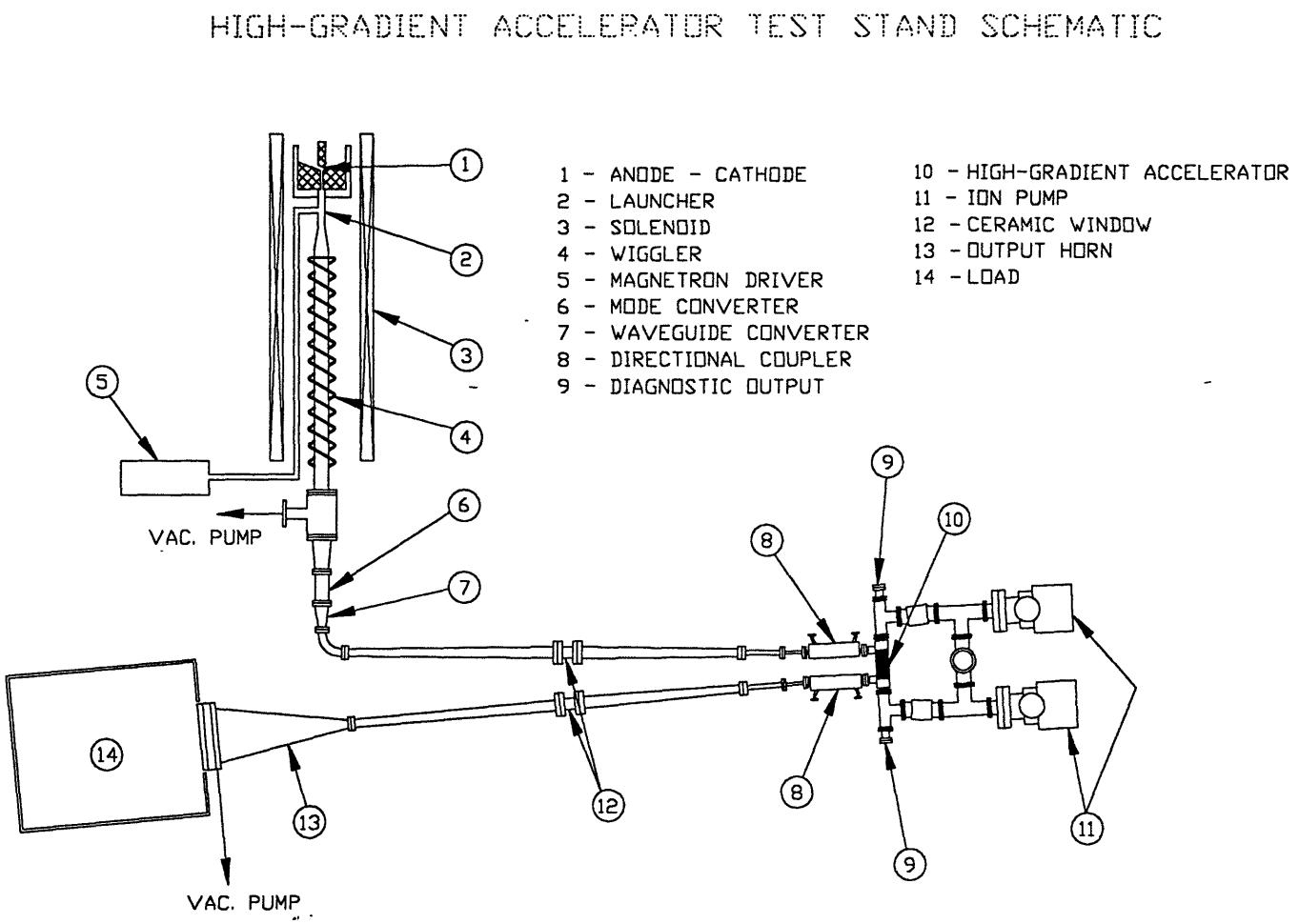

Figure 3-3: The schematic of the HGA testing setup.

The polarization converter was tested and squeezed at the LLNL T4325 microwave laboratory. It was connected [27] at one end to an electroformed circular waveguide tapering from an ID of 0.625 inch (to match the FEL output guide) to 0.550 inch (to match the standard circular waveguide size used for the squeezed section), and [29] at the other end to an electroformed transition from 0.550 inch ID circular guide to WR-28 rectangular guide (0.280×0.140 inch). Squeezing resulted in a 2.65 dB (84%) improvement in transmission through the three piece combination as compared to transmission with an unsqueezed circular waveguide section. The final insertion loss for the combination is 0.50 ± 0.10 dB.

3.3 High Power Testing

One of the goals of this experiment is to find the highest power level the structure could support without breakdown or some other process that would make it unsuitable for electron acceleration. In order to determine whether there is an undesirable process taking place in the HGA section and to try and learn about the process we had at our disposal several techniques.

3.3.1 Power Measurements

The most important diagnostic was the measurement of the incident, transmitted and reflected r.f. power. With use of crystal detectors and variable attenuators attached to the ports of the high vacuum directional couplers it was possible to sample the time profile of a radiation pulse at different time intervals: when it is just about to enter the accelerating structure (the *input* pulse-shape), when it exits the section (the *transmitted* pulse-shape), and of the radiation reflected back from the HGA (*reflected* pulse-shape). Any breakdown-like process would then be seen as a change in the transmitted and reflected power pulse-shapes.

A scan in the input power level ranging from 0.1 MW to about 35 MW was taken. At low powers the transmitted pulse resembled the input pulse in shape and the percentage difference in power magnitudes was equal to the 'cold' attenuation

as measured with a network analyzer (with very small $\sim$ 1 mW power levels). An example of input and transmitted power pulses at low input power level is given in figure 3-4.

As the power levels increased ($\sim$ 3 MW) the transmitted power pulse became shorter than the input power pulse in time duration. The early part of the transmitted power pulse still resembled the input pulse, while the transmitted power was attenuated stronger and stronger the closer it approached the end of the pulse. The transmitted power 'rolled off' at the end of the pulse. An example of input and transmitted power pulses at a medium input power level is given in figure 3-5.

At power levels from 20 MW and higher the transmitted power pulse shape became effectively independent of the input pulse shape. The examples of such pulses are shown in figures 3-6 and 3-7. The transmitted pulse peak power value was no longer proportional to that of the input pulse. The upper graph of figure 3-8 shows peak power in the transmitted pulse plotted vs. average power in the input pulse. With the increase of the input power, the transmitted power pulse saturated at a level of $\sim$ 14 MW. The reflected power shown in the lower part of figure 3-8 rises to a maximum of about 6 MW.

The plot of the FWHM of the transmitted pulse vs. the average power in the input pulse is shown in figure 3-9. The fraction of the power in the reflected pulse would be expected to grow as the input power level increased, because the amount of the input power transmitted through the HGA was seen to decrease with increasing input power levels.

It turned out to be only partly true. Power levels of the reflected pulse agreed with the cold test results when the input power level was small. The reflected power did grow to become comparable to the input power at high input power levels (see the bottom graph of figure 3-8). But this growth did not fully account for the difference in energy between the input and transmitted pulses.

Another representation of our data is in terms of the energy in the pulse obtained by integerating the measured power over the respective pulse widths. In figure 3-10 we present the dependence of the transmitted and the reflected energies on the

average power in the input pulse. Note that at high input energies (corresponding to power levels of 20 MW) the transmitted and reflected energies together account for only a half of the input energy. This leads to the conclusion that a substantial fraction of the radiation energy is dissipated inside the HGA.

3.3.2 X-ray and Visible Light measurements

The input and output couplers into the HGA are at right angles to the direction of acceleration as shown in figure 3-3. There are two sapphire windows, one on either end of the HGA. These windows are transparent to visible light and soft X-rays. We installed two photomultipliers just outside the windows in which detected visible light and/or soft X-rays.

Covering the aperture of one photomultiplier with black photographic tape resulted in photomultiplier sensitive to the X-rays only. Sheets of aluminum of varying thickness were used to attenuate the X-ray intensity and thereby remain on the linear part of the photomultiplier response curve.

The other photomultiplier was turned at 90^o to the HGA axis, and a plane mirror was installed in such a way that a visible photon coming out of the HGA along the axis of the structure would be redirected to hit the plate of the photomultiplier (see the photograph of the setup in figure 1-2). This removed contributions from soft X-rays so that only visible light was detected. Neutral density filters were placed in the path of the visible photons thereby assuring that the photomiltiplier was used in its useful, linear regime.

Both light and X-ray induced photomultiplier signals were recorded for a range of r.f. input powers (0.1 MW to 30 MW) from the FEL. In figure 3-11 we show plots of the maximum photomultiplier voltage from light and X-ray vs. average r.f. input power. Both light and X-ray generation starts around 1 MW of input power and continues to rise exponentially with input power thereafter. To demonstrate this exponential growth we present the photomultiplier voltage plots on a logarithmic scale, as shown in figure 3-12. The observed growth of both X-ray and visible light intensities begin around 1 MW of input power which correlates well with the energy

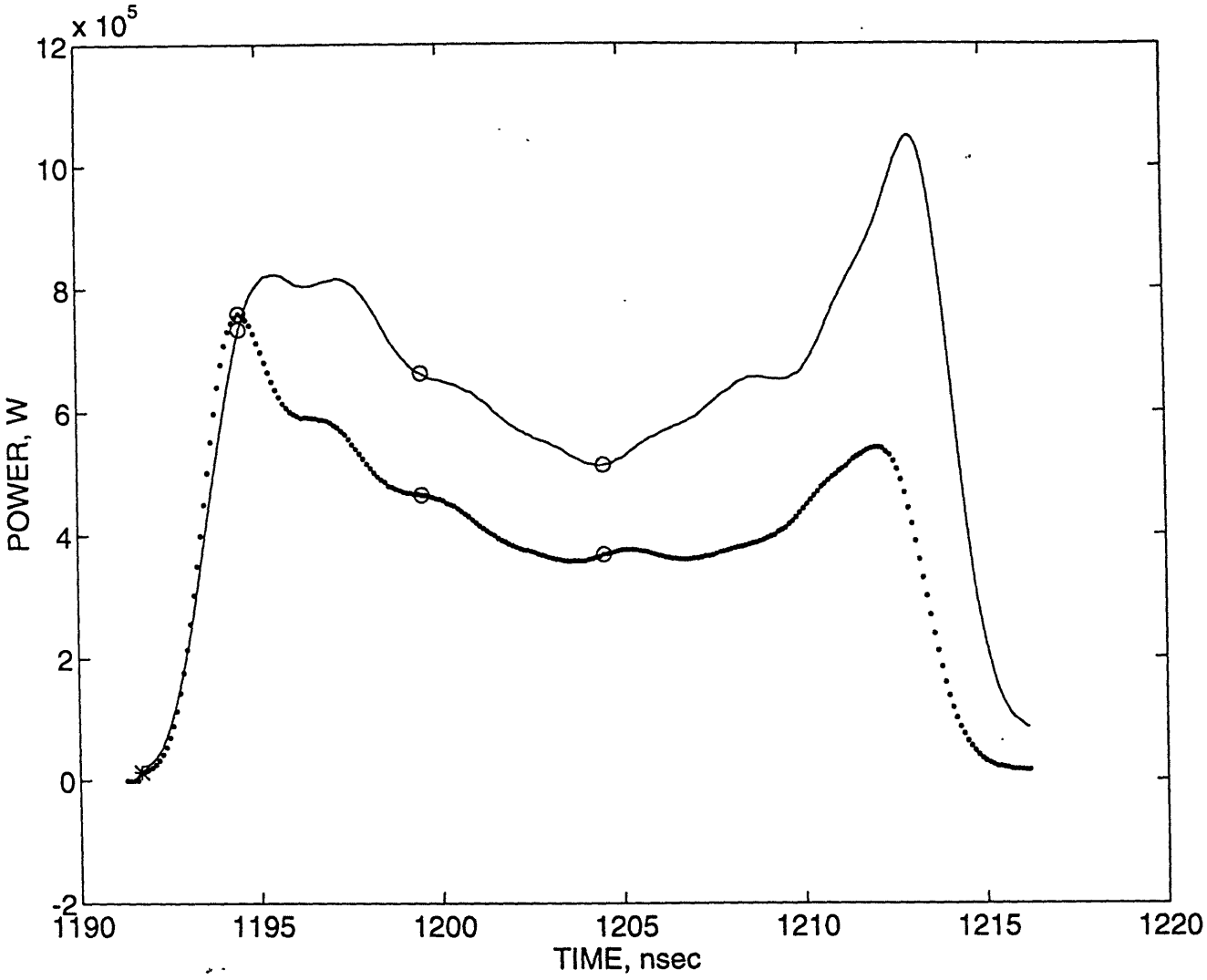

Figure 3-4: Transmitted and reflected power pulses at a low r.f. input power level, typically 100 kW.

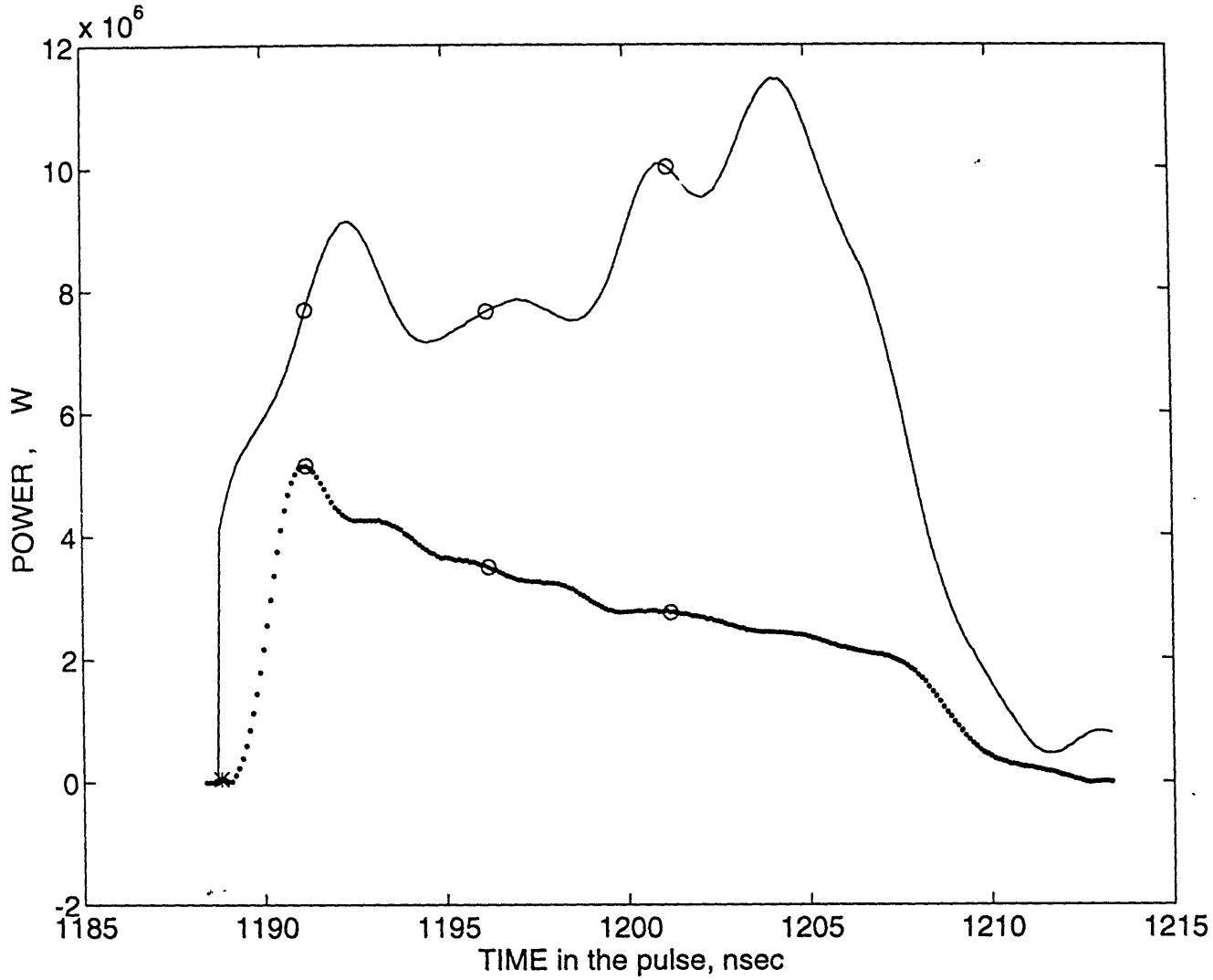

Figure 3-5: Transmitted and reflected power pulses at a medium input r.f. power level, typically 10 MW.

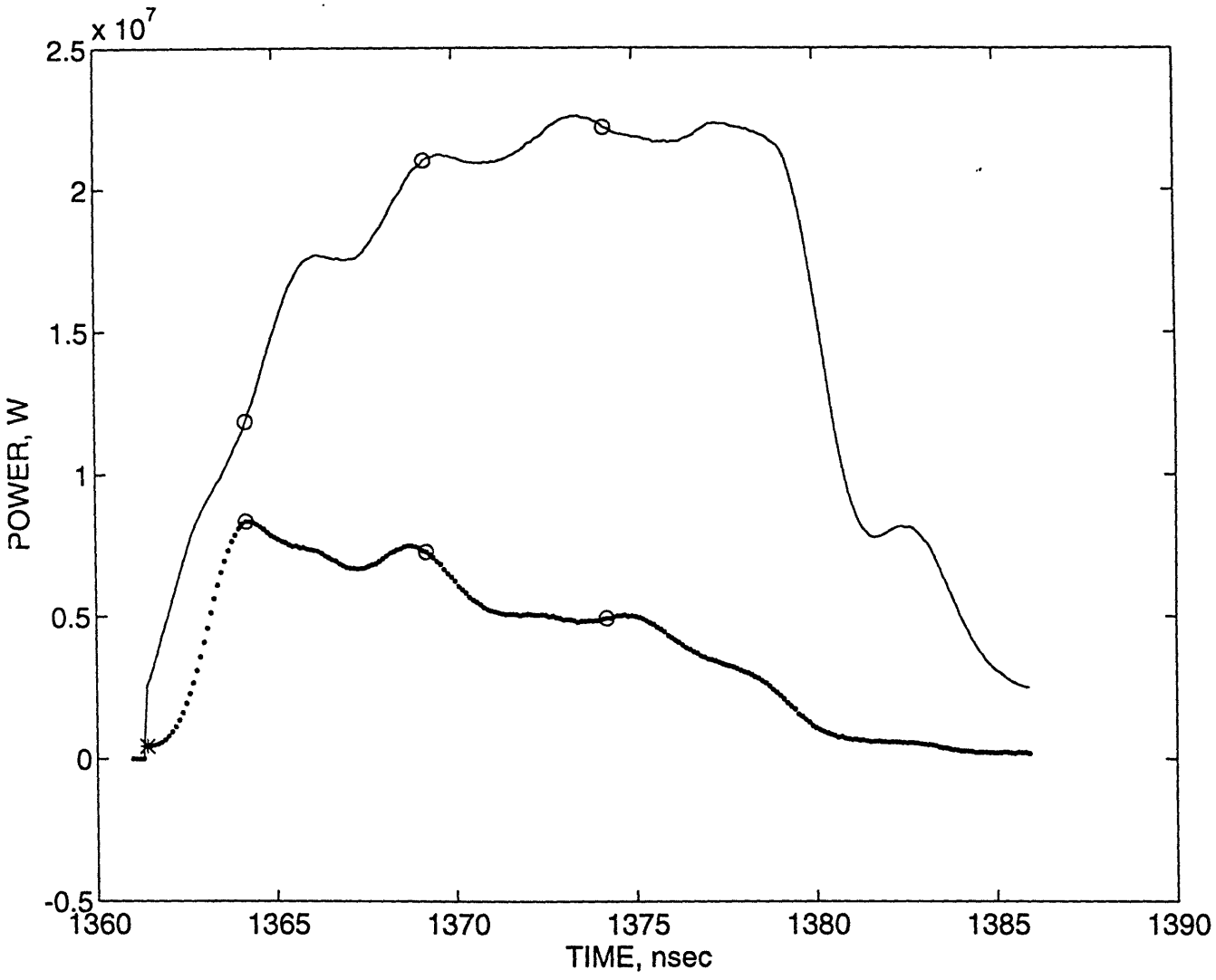

Figure 3-6: Transmitted and reflected power pulses at a high r.f. input power level of $\sim$ 20 MW.

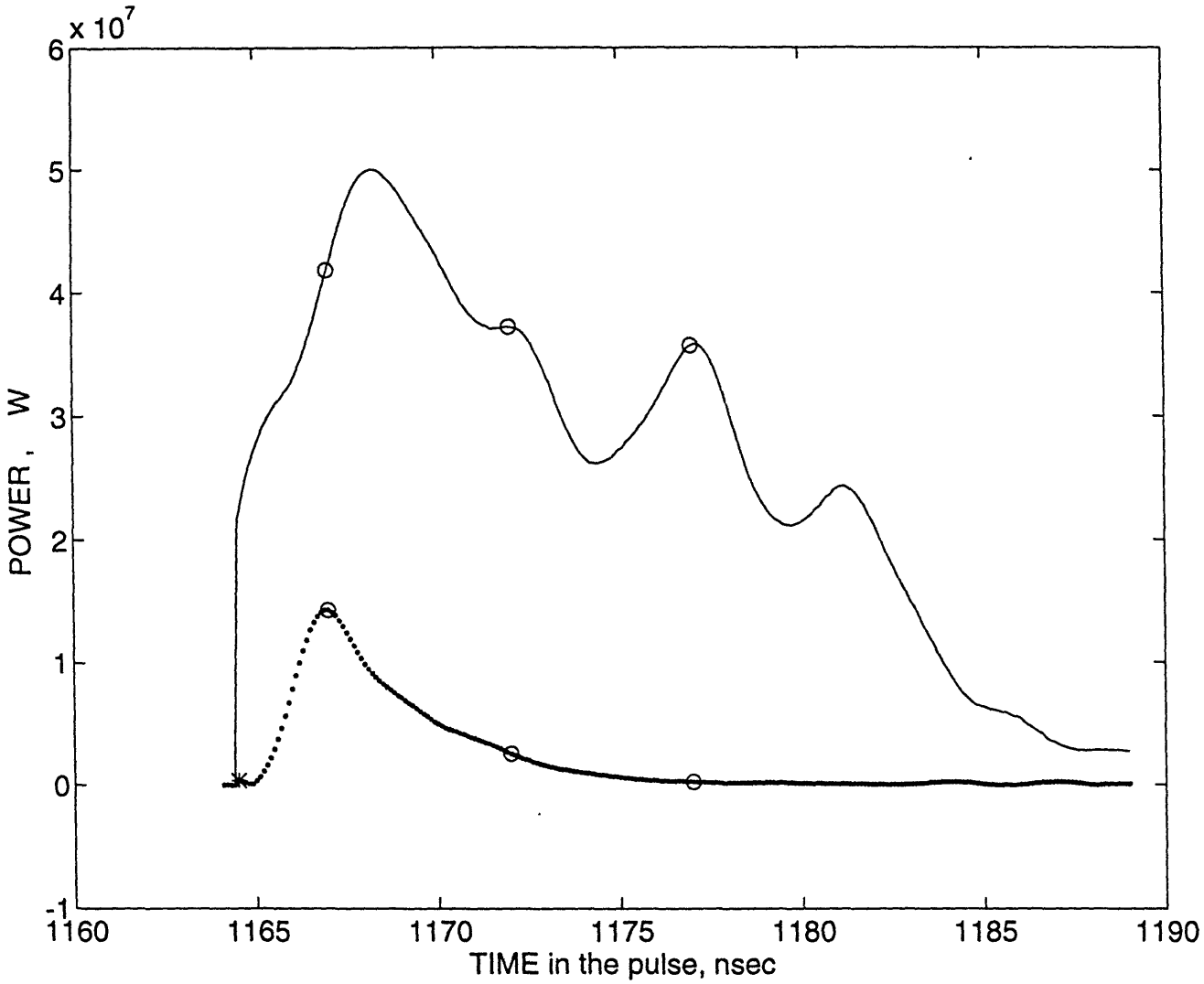

Figure 3-7: Transmitted and reflected power pulses at a high r.f. input power level, typically 50 MW.

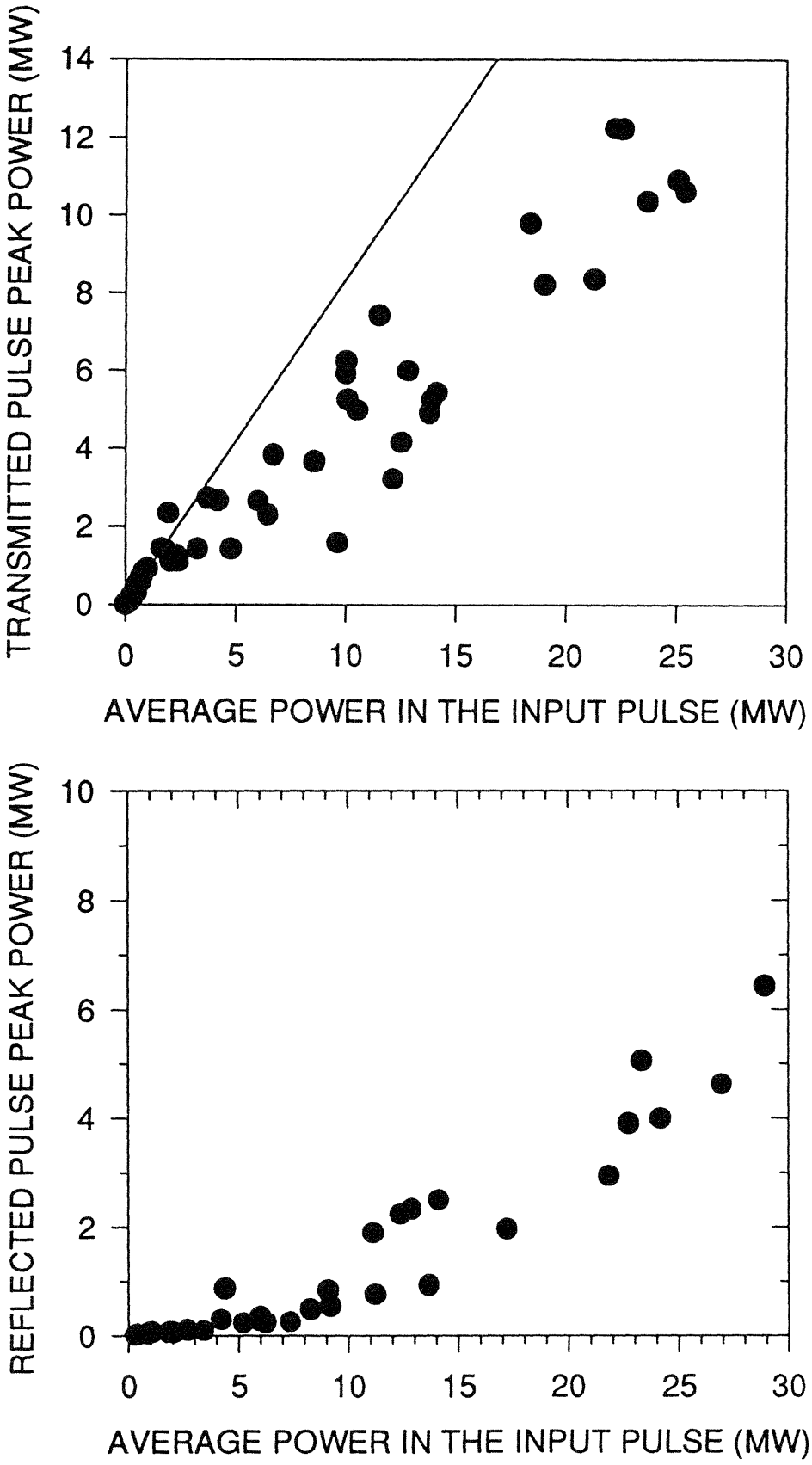

Figure 3-8: Peak power in the transmitted and reflected pulses plotted vs. average power in the input pulse.

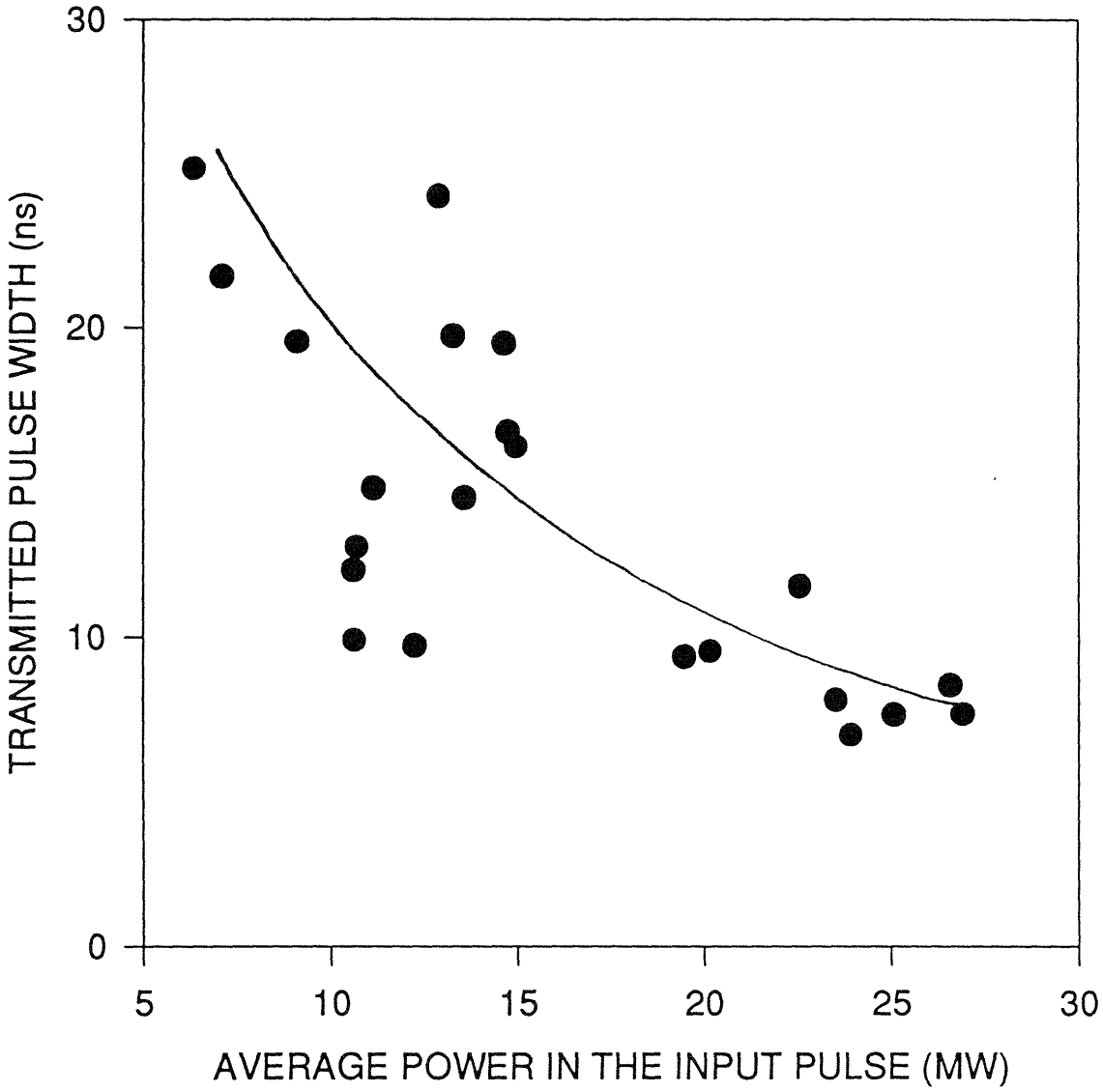

Figure 3-9: FWHM of the transmitted pulse vs. average input power.

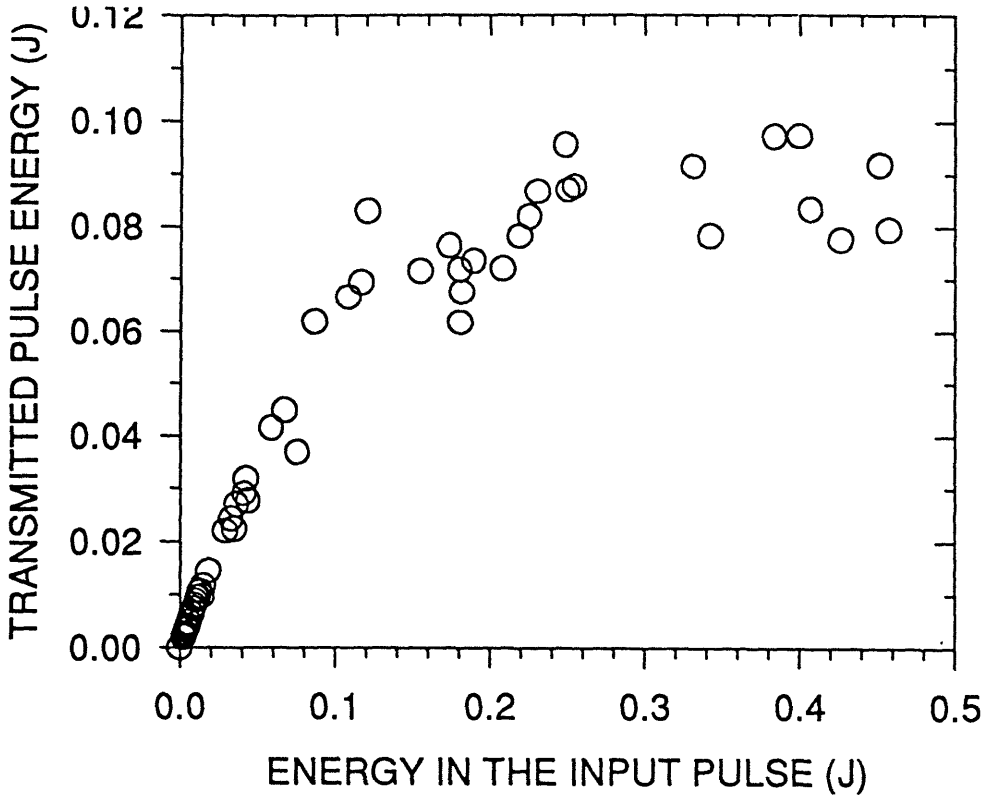

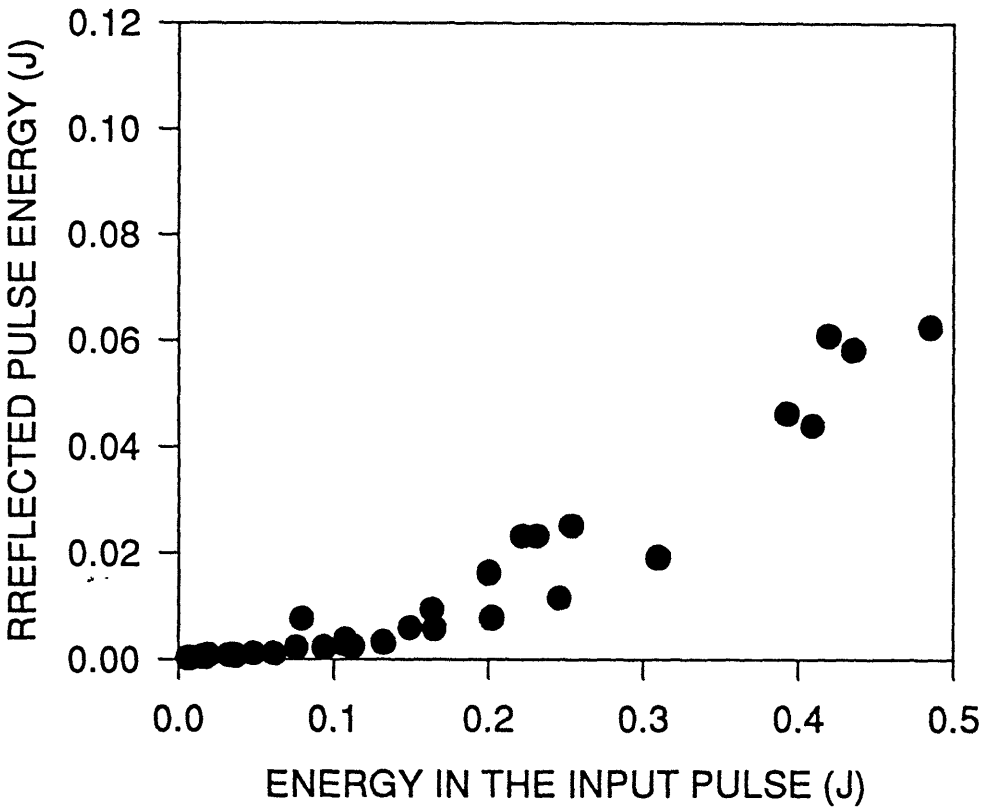

Figure 3-10: Transmitted and reflected energies vs. energy in the input pulse.

plots of figure 3-10.

3.4 Locating the problem

To verify that the breakdown takes place in the HGA and not in the measuring apparatus (the high vacuum directional couplers for instance) we substituted for the HGA a simple WR-28 waveguide section of about 30 cm long constructed at CERN/CLIC and evacuated it to a pressure $\sim 5 \times 10^{-7}$ Torr. The power diagnostic setup was left unchanged. As figures 3-13 and 3-14 demonstrate no pulse-shortening was observed. In addition, we measured the reflected power from a CERN/CLIC high power dump-load. We observed that reflections were low ($\sim 5\%$) and no pulse shortening was observed. Thus we conclude that the measuring apparatus does not contribute to pulse-shortening.

The fact that in the HGA the transmitted pulse is more attenuated at the later parts of the pulse (as seen in figure 3-7), and that the reflected power pulse reaches its peak value at the end of the pulse, suggests that there is a temporal growth of current (or of charge carriers) somewhere inside the HGA. One of the possible mechanisms for this growth is discussed below.

At all times there is a number of free charged particles inside a metal structure, either in the bulk or occluded on the walls. In the presence of high electric fields the field emission of electrons can be a dominating source. The high electric fields of the radiation pulse in the HGA would lead to acceleration of such charge carriers. The charged particles accelerated in this way will hit the metallic walls of the HGA and by some mechanism (such as, for instance, the secondary emission process) more charge carriers will be freed inside the HGA. If the losses of the carriers is less than the creation of new carriers an avalanche-like growth of current inside the HGA will result.

Part of the incident radiation will be dissipated by the carriers colliding with the walls of the HGA and the energy transfer to the growing number of carriers. Part of radiation will be reflected due to the impedance mismatch.

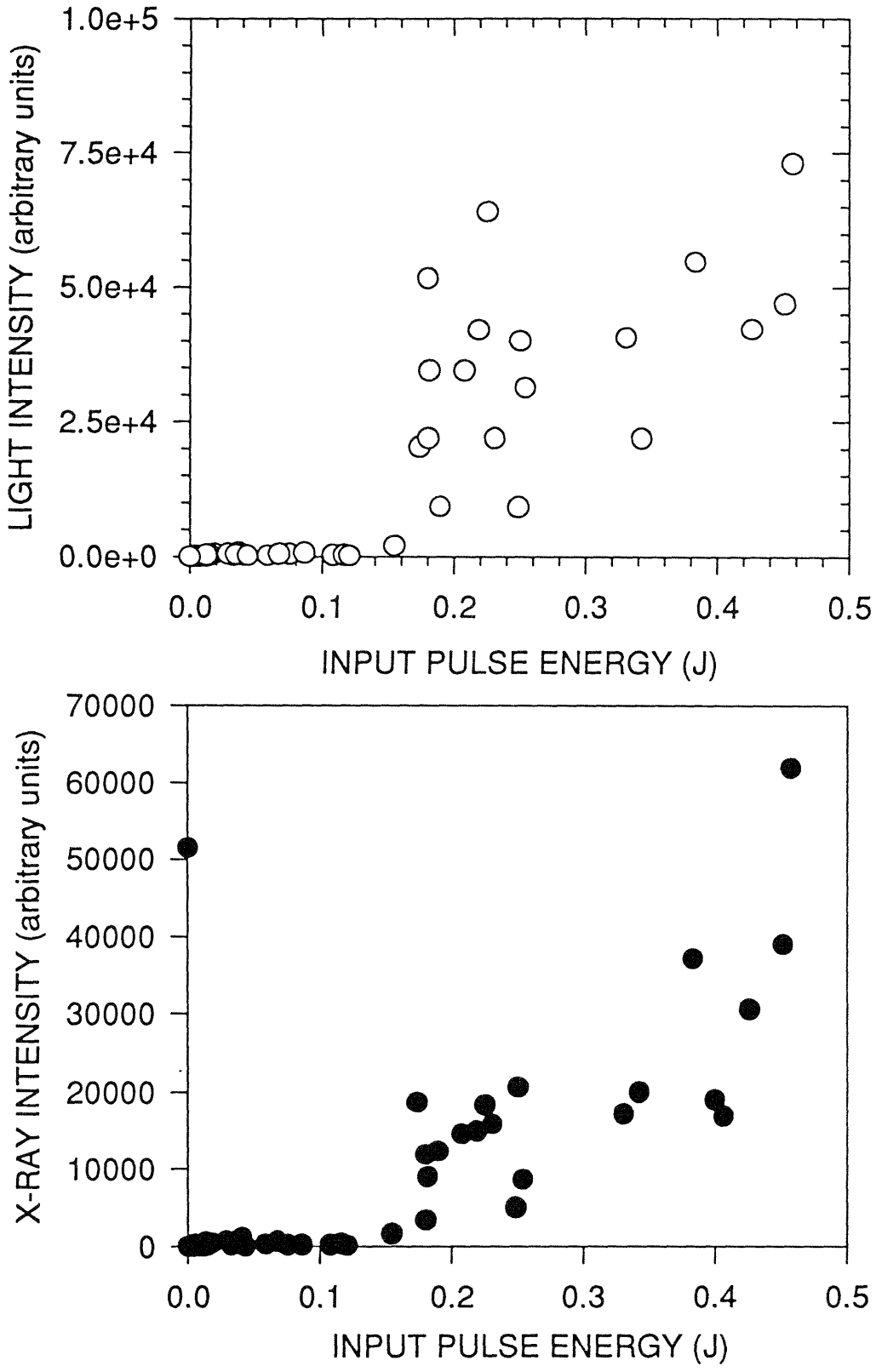

Figure 3-11: Light and X-ray induced photomultiplier signal vs. input energy.

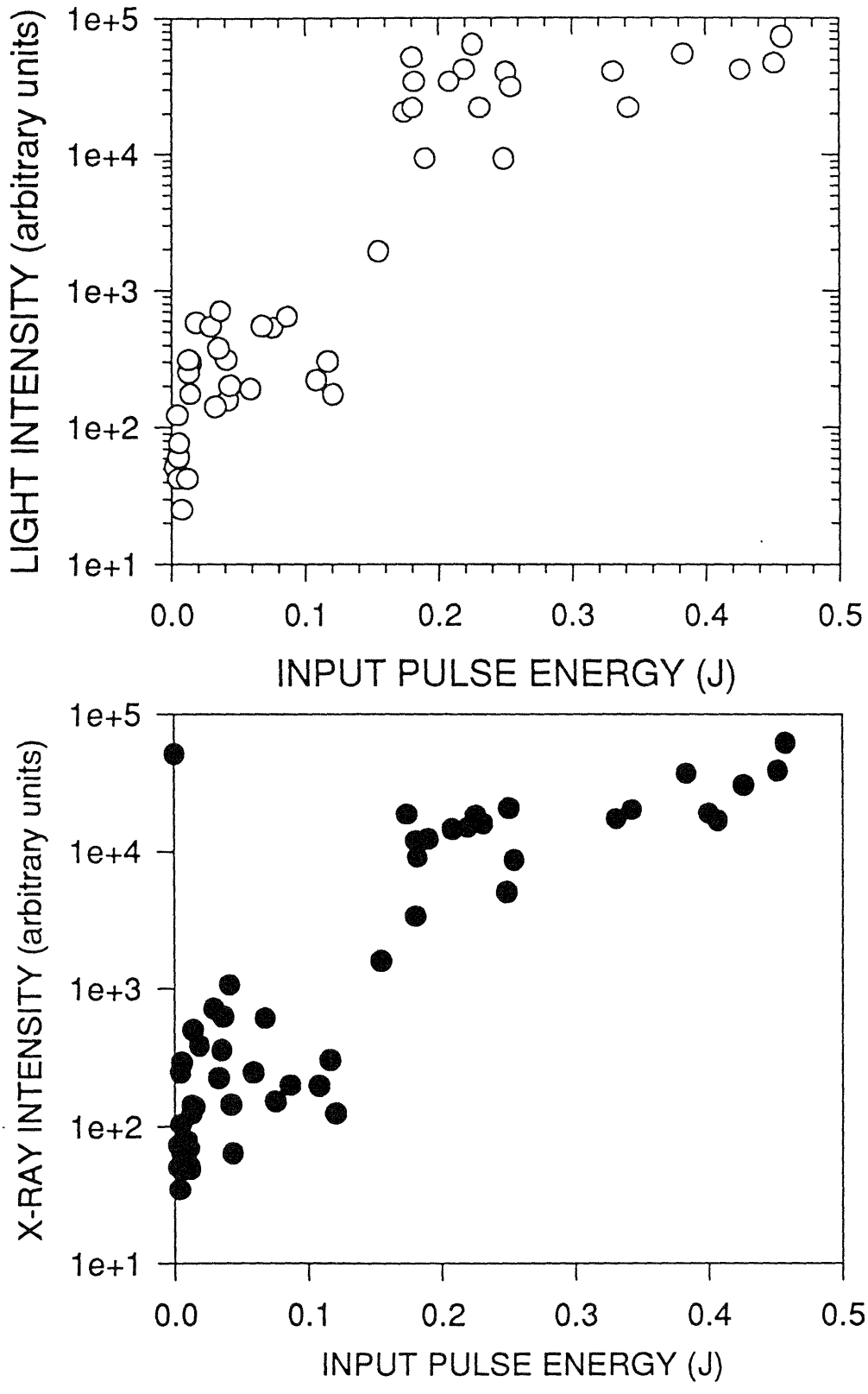

Figure 3-12: Light and X-ray induced photomultiplier signal vs. input energy, "log" scale.

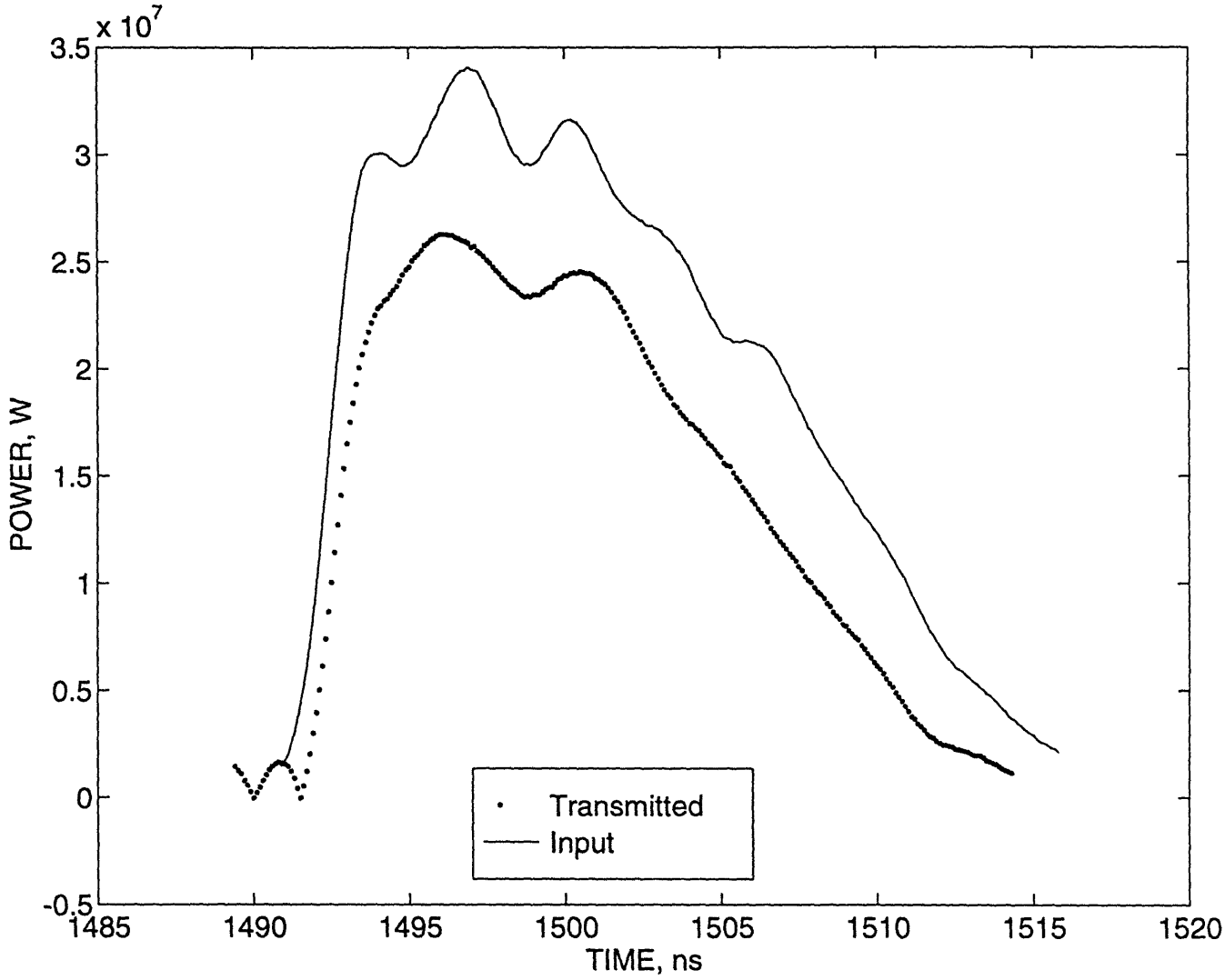

Figure 3-13: Typical transmitted and reflected pulses with a waveguide section in place of the HGA.

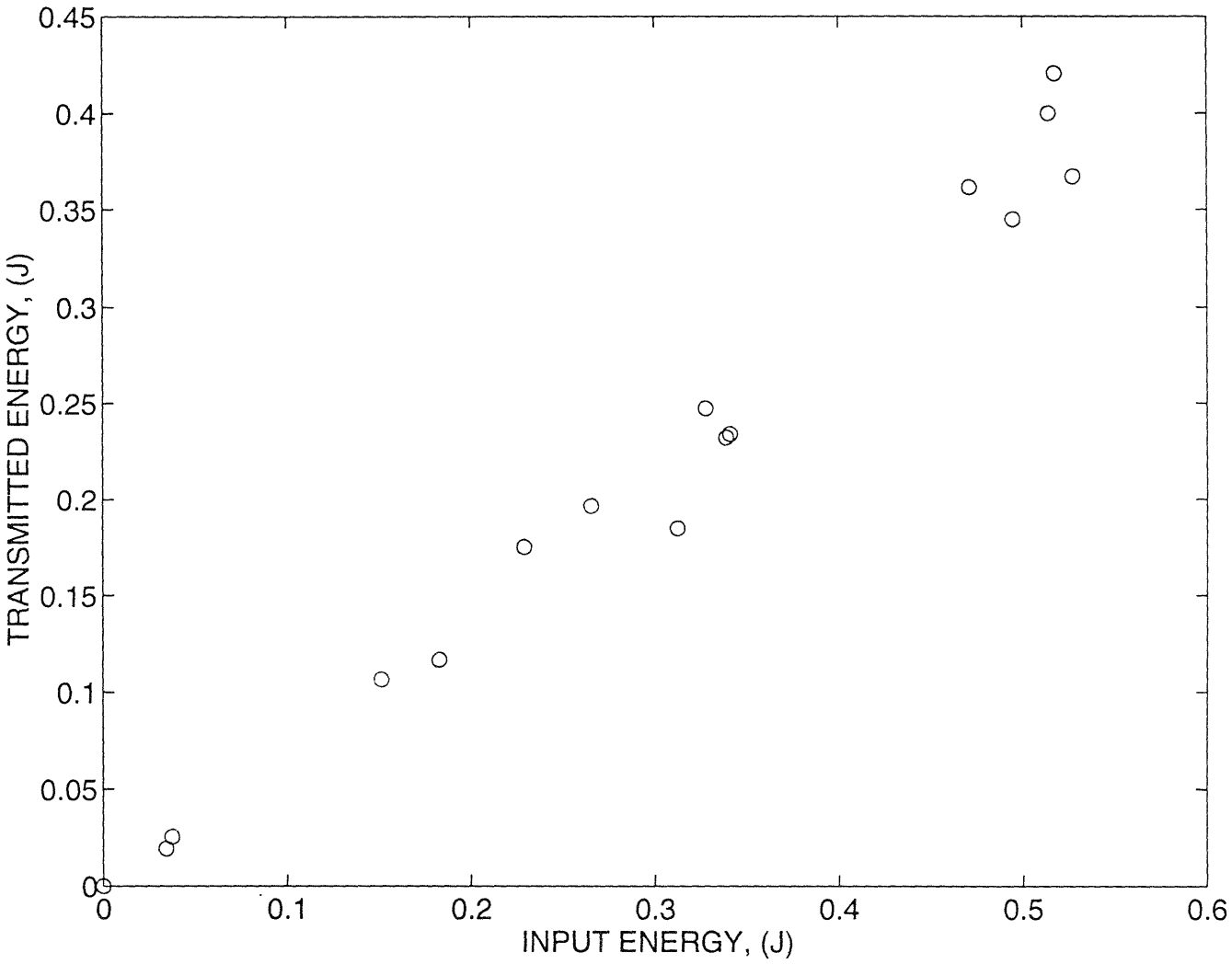

Figure 3-14: Transmitted energy vs. input energy with a waveguide section in place of the HGA.

To direct the future design efforts it is essential to know where exactly the pulse-shortening occurs: does it occur in the structure itself or do the side couplers to the section (not the directional couplers) break down first? To try to answer this question the following set of tests are conducted.

3.4.1 Magnetic Field Tests

The losses of charge carriers in an avalanche are partly due to the diffusion of the charged particles out of the "bad place". Constant magnetic fields perpendicular to the electric field of the radiation would change the trajectories of the carriers. The diffusion of the carriers out of the avalanche region will increase and the energy of the charged particles when they hit the walls of the HGA will decrease (at least for near to threshold powers). This could result in a change of the HGA performance.

A series of measurements were attempted where permanent magnets were placed in close vicinity of the HGA. These magnets create vertical magnetic fields (normal to the plane of the figure 3-3). 20 shots were taken at $\sim 20-30$ MW average input power without any magnets around the HGA. Then we took 20 shots at the same power levels with magnets placed on the side couplers to and from the structure (not the directional high-vacuum couplers). Then we took 20 shots with the magnets around the structure only, and another 20 with the magnets around both the structure and the couplers. The ratios of the output energy and input energy vs. averaged input power are shown in figure 3-15 a). Different symbols correspond to different ways we arranged the magnets. The ratio is definitely affected.

It is difficult to say exactly where the plasma formation is concentrated, but the effect of placing the magnets around the couplers (those create rather localized fields ~ 400 G) indicates that the couplers is one of the areas that contribute to the pulse-shortening.

High longitudinal magnetic fields ~ 5 kG were generated inside the structure by a solinoidal coil wound around it (figure 3-15 b). Virtually no change in the energy ratio could be seen.

In conclusion, transverse magnetic fields ~ 400 G in the couplers and/or in the

structure itself affect the pulse shortening, while large $\sim$ 5 kG longitudinal magnetic fields in the structure make little or no difference.

3.4.2 Operating at a Different Frequency

To further confirm that there is an undesirable process in the input side coupler to the HGA we detune of the FEL off the 0.5 GHz wide transmission band of the HGA to a new frequency $f = 33.682$ GHz.

The 33.682 GHz radiation couples to an evanescent mode in the structure. The major portion of the pulse is reflected, with only about 10% of the incident energy transmitted through the structure at this frequency. Thus the electric field gradients inside the structure itself are now much smaller than those in the input coupler.

If the coupler, rather than the structure, is the cause of the pulseshortening, the pulse shortening should be seen at the detuned frequency. Indeed, strong pulse-shortening was observed in reflected pulses. The graph of the FWHM of the reflected pulse vs. average energy in the input pulse is shown in figure 3-16 a. The reflected and transmitted energy vs. input energy is seen in figure 3-16 b. For high input energies $\sim$ 0.6 J the reflected energy constitutes only 20% of the input and the transmitted energy accounts for maybe another 2%. A large fraction of the input energy is thus dissipated.

The last two subsections have shown that there are strong indications that it is mainly in the input coupler that the pulse shortening takes place.

3.5 Investigation of the Feasibility of Conditioning

In this section we examine if the performance of the HGA improves with the number of shots, so that future conditioning could perhaps eliminate the pulse shortening. When fabricated a high gradient system may benefit from Conditioning [30]. Conditioning means that a large number of shots of radiation through the system is taken with

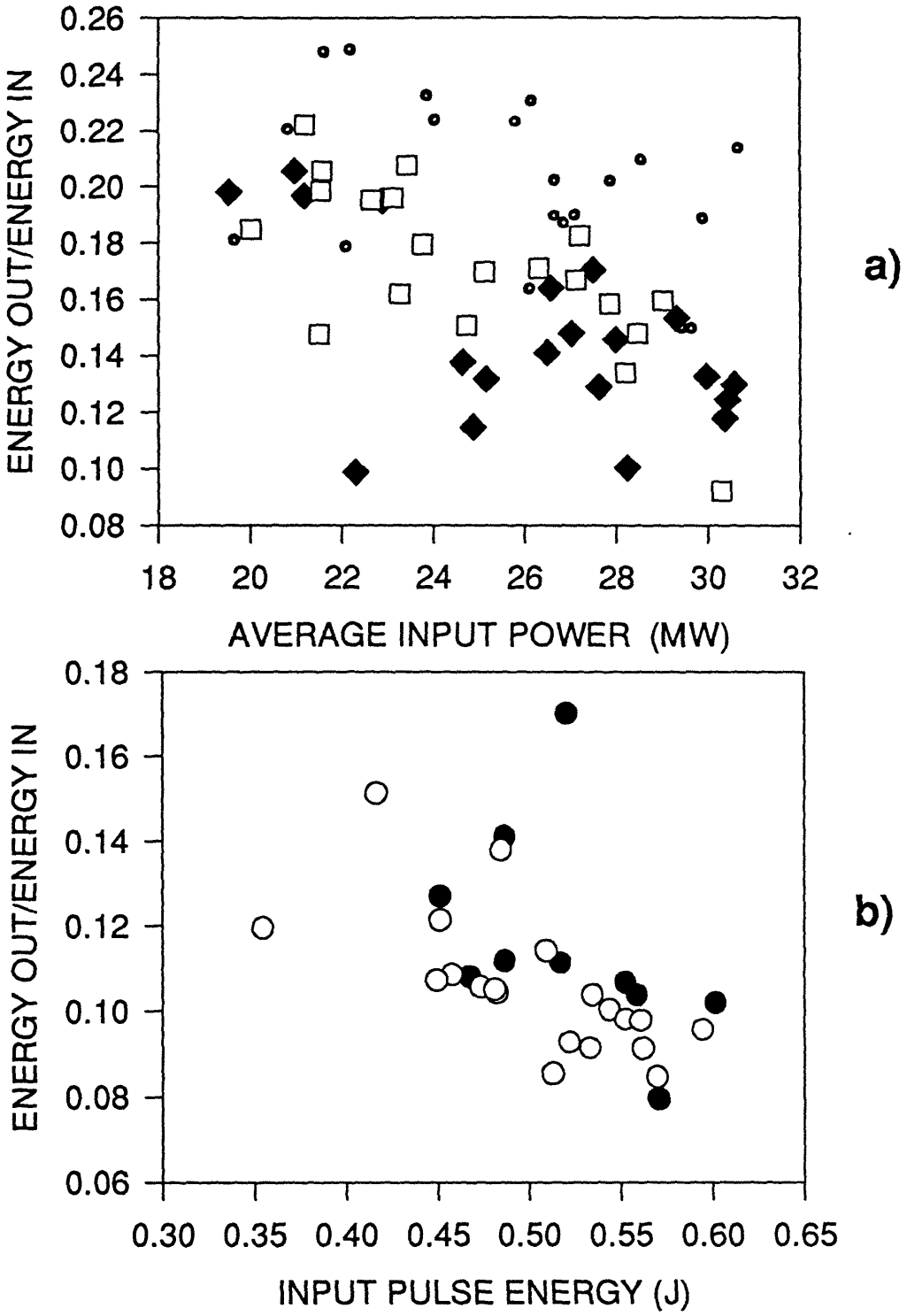

Figure 3-15: Measurements of pulse shortening (ratia of energy transmitted to energy incident) as a function of input pulse power (a) and energy (b). a) Dots correspond to no external magnetic field; filled diamonds show measurements with $\sim$ 450 G of constant magnetic field on the axis of the HGA and no magnetic field on the couplers; hollow squares are for data taken with the magnets around the couplers only. b) The filled circles represent data with zero field, the hollow circles are with high axial magnetic field $\sim$ 5 kG on the structure.

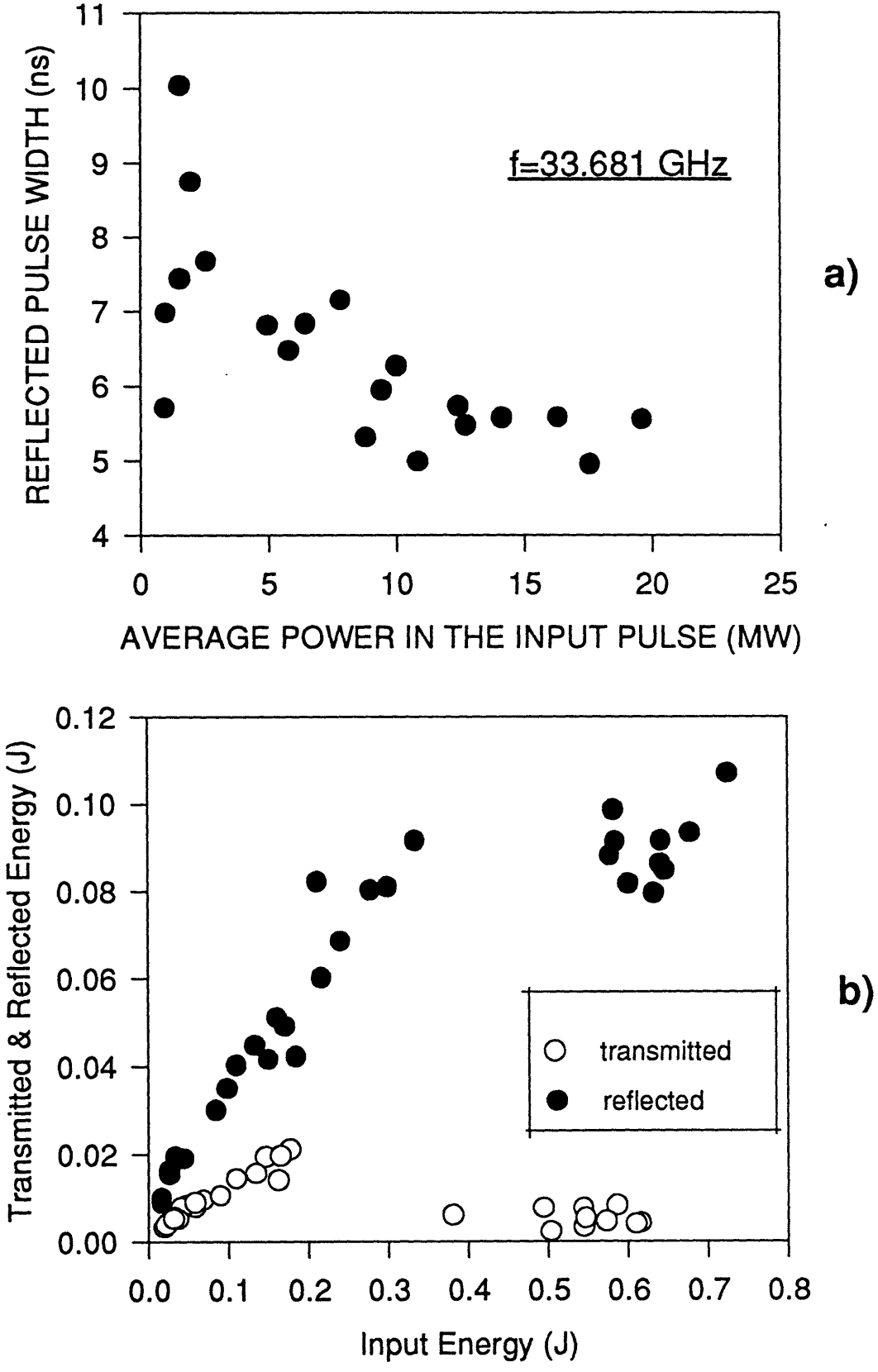

Figure 3-16: HGA studies at the detuned magnetron frequency f=33.681 GHz. a) FWHM of the reflected pulse vs.average input power. b) Energy in the reflected and transmitted pulses vs. input energy.

increasing r.f. power input. It effectively cleans the system by small discharges with the incident pulse power slowly increased as the discharges start to subside. In this way, gas can be removed from the surfaces while avoiding serious surface damage that could take place had power been injected initially at high levels.

The estimated number of shots required for conditioning varies from a hundred thousand to several millions. It did not seem feasible to fully condition the HGA using the existing FEL (for it produces only one shot every two-three minutes and is manually operated). For example, the conditioning of an 11.4 GHz 30-cell HGA at the LLNL ARC facility using $\sim$ 40 ns pulses at 1-4 pps repetition rate required more than 500,000 shots [30]. It is noted, however, that the rate of improvement was much greater during the first 5,000-10,000 shots. This motivated the following test of the feasibility of conditioning in our HGA.

A power scan was made of the output and input pulses with the input power level ranging from 0.1 to 30 MW. An attempt to condition the structure was made with some 800 shots at power levels gradually increasing from 3-5 MW to around 20 MW were taken. The power scan was then repeated.

To quantitatively characterize the amount of pulse-shortening we took three simultaneous measurements of input and transmitted power at three distinct times: at the first maximum of the transmitted power pulse, five nanoseconds later in the pulse, and ten nanoseconds later. Figures 3-17 and 3-18 a) show the dependence of the output pulse power values on the input pulse power values occurring at the same time in the pulse. The measurements taken before the conditioning are drawn as black circles, those taken after are hollow. One can see that after conditioning the power values at 5 and 10 nanoseconds are closer to the input power values than before conditioning. The values at the first maximum of the output power seem to follow the input power values well in both cases.

Figure 3-18 b) shows plots of output vs. input energy before and after the conditioning. One observes a definite improvement in transmission.

There is evidence in favor of possibility of conditioning, provided a high enough power and repetition rate source at 33 GHz is available.

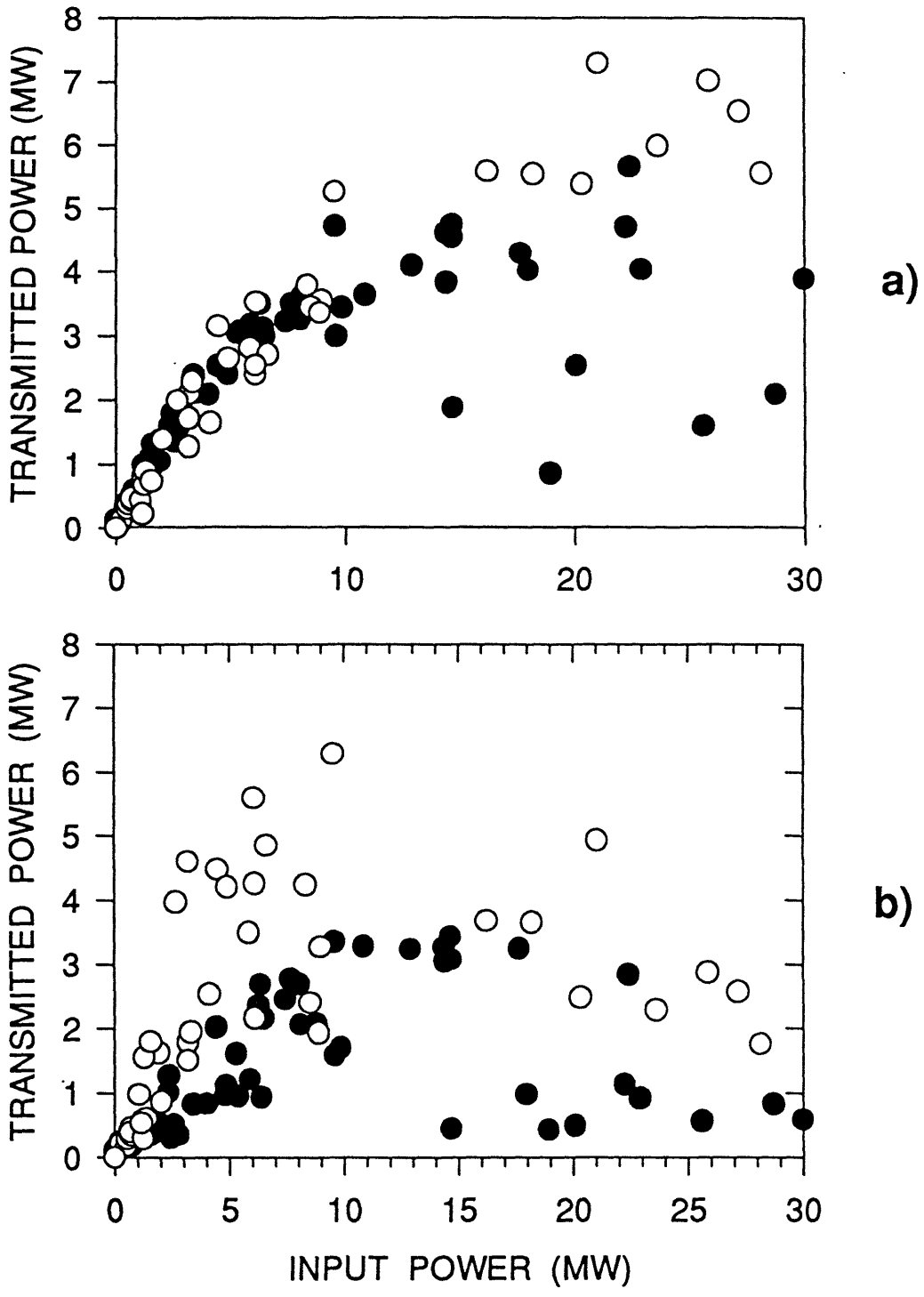

Figure 3-17: The simultaneous power measurement in the transmitted and input pulses. The black dots are before an attempt to condition, the hollow dots are after it. (a) corresponds to 5 ns after the first maximum of the transmitted pulse, (b) corresponds to 10 ns after the first maximum.

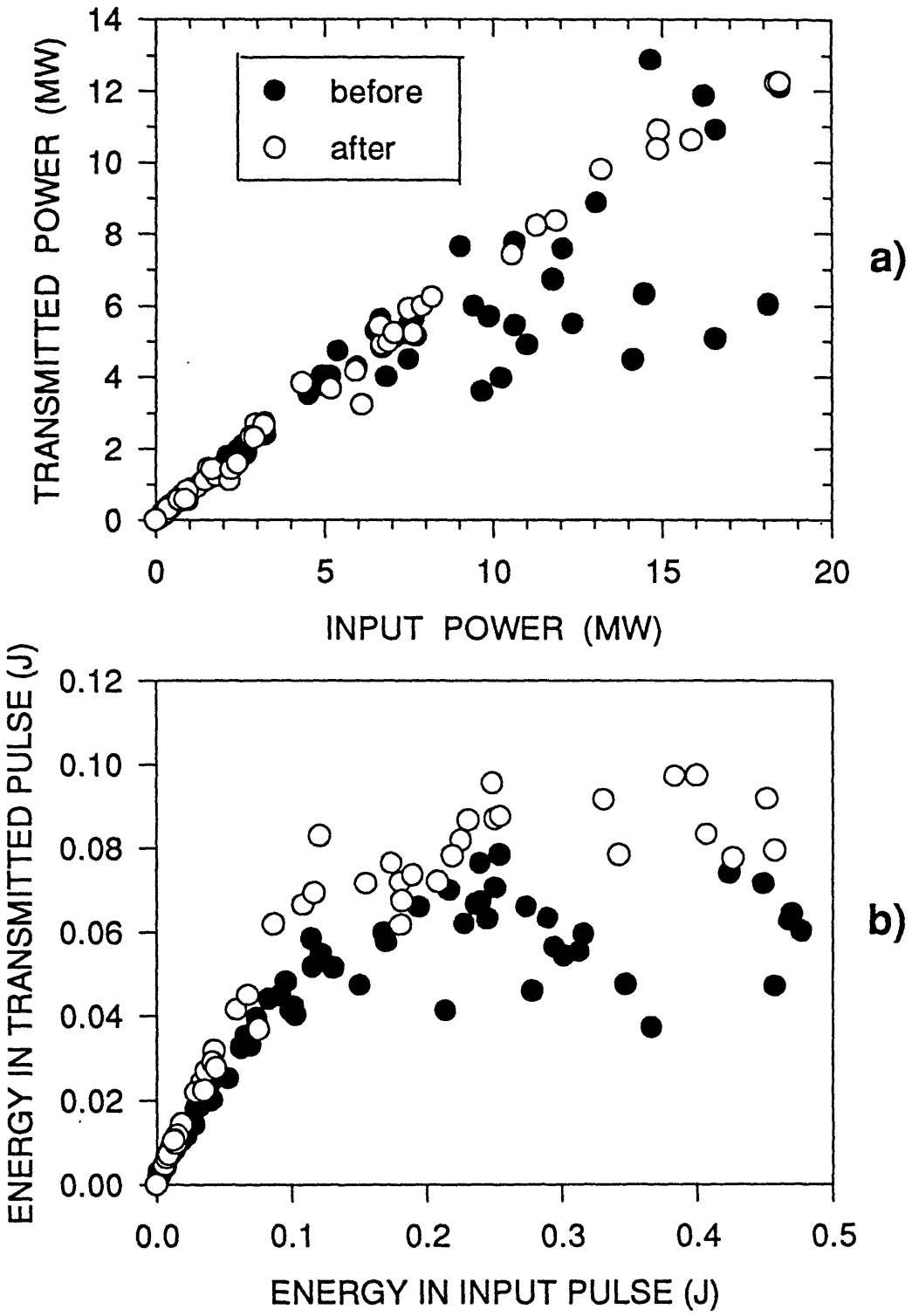

Figure 3-18: Black dots correspond to the data taken before 800 conditioning shots, hollow dots are after the attempt to condition. a)The simultaneous power measurement in the transmitted and input pulses. The values are taken at the first maximum of the transmitted power. b)Transmitted vs. input energy.

Chapter 4

Conclusions

In Chapter 2 of this thesis detailed measurements of the temporal and spatial phase behavior of the MIT's pulsed Free Electron Laser amplifier in three different operating regimes was described. We believe these were the first such experiments in the high gain regime. Knowledge of the temporal behavior of phase allows determination of instantaneous frequency shifting of the device. The sensitive interferometric method used confirms an earlier, but cruder, investigation [6, 7, 25].

The reversed field regime [16, 17, 18, 7] proved to be best operating regime of the FEL, with a combination of both high power (60 MW) and low frequency shift ($\sim$ +8 MHz/m) that virtually does not change throughout the bulk of the pulse.

The measured temporal chirping characteristics depend critically on voltage and current pulse shapes and on the relative timing between the voltage, current, and onset of FEL radiation. The results are in agreement with theoretical predictions [23].

Detailed measurements of the spatial variations of the phase and r.f. power with interaction length are also presented, and compared with time-independent simulations [8]. The overall agreement is fair. The simulation is seen to better agree with the data if in each regime beam energy and emittance are adjusted (by 10% and 100% respectively). However we believe that such variances assumed in the code lie outside acceptable uncertainties in the experiments.

The high power testing of a 33 GHz High Gradient Accelerating Structure yielded

the maximum accelerating gradient of 65 MeV/m. A pulse-shortening phenomenon was observed for power levels > 3 MW . At the highest power levels the output pulse length (about 5 nsec) was about one quarter of the input pulse length. Various tests suggest that these undesirable effects occur in the input coupler to the HGA. Light and X-ray production inside the HGA have been observed.

A study of feasibility of conditioning (limited by the low repetition rate of our FEL) suggest that conditioning is a likely candidate for improvement of the HGA power handling performance.

Bibliography

[1] G. Bekefi. Coherent free-electron sources. In A. Sen and P.K. Kaw, editors, *Proceedings 1989 International Conference on Plasma Physics*, 1989.

[2] C.W. Roberson and P.Sprangle. A review of free-electron lasers. *Phys. Fluids B*, 1(3), 1989.

[3] T.C. Marshall. *Free-Electron Lasers.* Macmillan, New York, 1985.

[4] K.-J. Kim and M. Xie. *Nucl. Instr. and Methods A*, 304:146, 1991.

[5] T.J. Orzechowski, E.T. Scharlemann, and D.B Hopkins. Measurement of the phase of the electromagnetic wave in a free-electron laser amplifier. *Phys. Rev. A*, 35:2184, 1987.

[6] M.E. Conde, C.J. Taylor, and G. Bekefi. Observations of frequency upshift in a pulsed free-electron laser amplifier. *Phys. Fluids B*, 5(7):1934, 1993.

[7] M.E. Conde. *A 33 GHz Free Electron Laser Amplifier with Reversed Axial Guide Magnetic Field.* PhD thesis, MIT, 1992.

[8] G. Zhang, G. Shvets, and J.S. Wurtele. Theoretical study of free electron lasers with reversed guide field. *Nucl. Instr. Meth. Phys. Research Section A*, 331:472, 1993.

[9] W.D. Kilpatrick. Criterion for vacuum sparking designed to include both r.f. and d.c. *The Review of Scientific Instr.*, 28(10), 1957.

[10] A.M. Sessler. The Free Electron Laser as a Power Source for a High-Gradient Accelerating Structure. In *Laser Acceleration of Particles (AIP Conf. Proc.)*, number 91 in American Institute of Physics, New York, page 154, 1982.

[11] R. Bossart et. al. Performances obtained with the CERN Linear Collider Test Facility (CTF). In *EPAC 94, Proceedings of the Fourth European Particle Accelerator Conference*, volume 1, page 680, 1994.

[12] Y. Baconnier et. al. The CERN Linear Collider Test Facility. In *paper presented at the 1992 Linear Accelerator conference [Ottawa], CERN PS 92-49[LP].*

[13] L. Friedland. Electron beam dynamics in combined guide and pump magnetic fields for free electron laser applications. *Phys. Fluids*, 23:2376, 1980.

[14] P. Diament. Electron orbits and stability dynamics in realizable and unrealizable wigglers of free electron lasers. *Phys. Rev. A*, 23:2537, 1981.

[15] H.P. Freund, P. Sprangle, D. Dillenburg, E.H. Jornada, R.S. Schneider, and B. Liberman. Coherent and Incoherent Radiation from Free Electron Lasers with an Axial Guide Field. *Phys. Rev. A*, 24:1965, 1981.

[16] M.E. Conde and G. Bekefi. Experimental Study of a 33.3 GHz Free Electron Laser Amplifier with a Reversed Axial Guide Magnetic Field. *Phys. Rev. Lett.*, 67:3082, 1991.

[17] M.E. Conde and G. Bekefi. High efficiency 33.3 GHz free electron laser amplifier with a reversed axial guide magnetic field. *Nucl. Instr. Meth. Phys. Research Section A*, 318:109, 1992.

[18] M.E. Conde and G. Bekefi. Amplification and Superradiant Emission from a 33.3 GHz Free Electron Laser Amplifier with a Reversed Axial Guide Magnetic Field. *IEEE Trans. on Plasma Science*, 20(3):240, 1992.

[19] J. Fajans. End effects of a bifilar magnetic wiggler. *J. Appl. Phys.*, 55(43), 1984.

[20] K.R. Chu and A.T. Lin. Harmonic gyroresonance of electrons in combined helical wiggler and axial guide magnetic fields. *Phys. Rev. Lett.*, 67:3235, 1991.

[21] J. Fajans, D.A. Kirkpatrick, and G. Bekefi. Off-axis electron orbits inrealistic helical wigglers for free-electron-laser applications. *Phys. Rev. A*, 32:3448, 1985.

[22] C. Chen and R.C. Davidson. Chaotic Particle Dynamics in Free Electron Lasers. *Phys. Rev. A*, 43:5541, 1991.

[23] G. Shvets and J.S. Wurtele. Frequency Shifting Phenomena In Free Electron Lasers. *Nucl. Instr. Meth. Phys. Research Section 1*, 1(1):157, 1994.

[24] R.E. Collin. *Foundations of Microwave Engineering*, page 282. McGraw-Hill, New York, 1966.

[25] G. Bekefi, B. Chen, M.E. Conde, I. Mastovsky, K. Ricci, C.J. Taylor, and P. Volfbeyn. Observation of Frequency Chirping and Phase of a Free Electron Laser Amplifier. *Nucl. Instr. Meth. Phys. Research Section 1*, 1993.

[26] R.W. Kuenning, A.M. Sessler, and J.S. Wurtele. Laser Acceleration of particles. In C. Joshi and T. Katsouleas, editors, *AIP, New York*, Malibu, CA, 1985.

[27] J. Haimson. Final Report High Gradient 33.3 GHz Electron Accelerator. Technical Report HRC-764-3, Haimson Research Corporation, 1987.

[28] J.R. Pyle. Circular Polarizers of Fixed Bandwidth. *IEEE Trans. Microwave Theory and Techniques, MTT-12*, 5:557, 1964.

[29] J. Haimson and B.Mecklenburg. Design and Construction of a 33 GHz Brazed Accelerator Components. In *Proc. Mar. 16-19, 1987 IEEE Part. Accel. Conf.,IEEE Cat. No. 87CH2387-9*, volume 3, page 1928, 1987.

[30] D.B. Hopkins and G.T. Conrad. Plans for testing the 33.3 GHz high gradient accelerator at MIT. CP-49 september 27, 1989.